

Solution structure and dynamics of the mitochondrialtargeted GTPase-activating protein (GAP) VopE by an integrated NMR/SAXS approach

Journal:	Protein Science
Manuscript ID	PRO-21-0309.R1
Wiley - Manuscript type:	Full-Length Papers
Date Submitted by the Author:	17-Jan-2022
Complete List of Authors:	Smith, Kyle; Xilio Therapeutics Lee, Woonghee; University of Colorado Denver, Chemistry Tonelli, Marco; University of Wisconsin-Madison, National Magnetic Resonance Facility Lee, Yeongjoon; University of Colorado Denver, Chemistry Light, Samuel; University of Chicago Biological Sciences Division, Microbiology Cornilescu, Gabriel; National Cancer Institute, Advance Technology Research facility Chakravarthy, Srinivas; Argonne National Laboratory, Biophysics Collaborative Access Team
Keywords:	GTP hydrolysis, Vibrio Cholerae, mitochondrial dynamics, small-angle x-ray scattering, relaxation dispersion, helical bundle, catalytic arginine finger, T3SS secretion system, YopE, ExoS

SCHOLARONE™ Manuscripts Solution structure and dynamics of the mitochondrial-targeted GTPase-activating protein (GAP) VopE by an integrated NMR/SAXS approach

Kyle P. Smith 1,2*\(\psi\), Woonghee Lee 3*, Marco Tonelli 4, Yeongjoon Lee 3, Samuel H. Light 5, Gabriel Cornilescu 6, Srinivas Chakravarthy 7

- 1 Current, Xilio Therapeutics, Waltham, MA, 02451, USA
- 2 Former, Department of Cell & Developmental Biology, Northwestern University Chicago, IL 60611, USA
- 3 Department of Chemistry, University of Colorado-Denver, Denver, CO 80204, USA
- 4 National Magnetic Resonance Facility at Madison, Department of Biochemistry, University of Wisconsin-Madison, Madison, WI 53706, USA
- 5 Department of Microbiology, University of Chicago, Chicago, IL 60637, USA
- 6 Advanced Technology Research Facility, Frederick National Laboratory for Cancer Research, Leidos Biomedical Research, Inc., National Cancer Institute, National Institutes of Health, Frederick, MD 21701, USA
- 7 Biophysics Collaborative Access Team, Argonne National Laboratory, Argonne, IL 60439, USA

+ Corresponding Author, kyle.smith.phd@gmail.com

Correspondence:

Kyle P. Smith 104 Hope Ave., Apt. 104 Waltham, MA 02453 908-672-5134 kyle.smith.phd@gmail.com

^{*}Co-first author

Running Title:

"NMR Structure of VopE"

Total number of manuscript pages, supplementary pages, tables, and figures:

34

Manuscript pages: 18
Supplementary pages: 10
Tables: 1
Figures: 5

<u>Description of supplementary material and file names:</u>

- 1) Supplementary Figure 1: Hydrolysis of GTP is catalyzed through GAP arginine "finger"
- 2) Supplementary Figure 2: VopE sequence alignment with other ToxGAPs
- 3) Supplementary Table 1: MALS and SAXS scattering values.
- 4) Supplementary Figure 3: ¹H/¹⁵N HQSC of VopE.
- 5) Supplementary Figure 4: Correlation between calculated and experimental RDC values
- 6) Supplementary Figure 5: Sequence and secondary structure alignment
- 7) Supplementary Figure 6: Electrostatic Surface Representation of VopE
- 8) Supplementary Figure 7: Overlay of VopE fold to that of other ToxGAPs
- 9) Supplementary Figure 8: Dispersion curves for the residues with R_{ex} greater than 6 s⁻¹
- 10) Supplementary Figure 9: Representative SDS-PAGE and preparative SEC purity for recombinantly expressed and purified VopE

Abstract

The bacterial pathogen *Vibrio cholerae* use a type III secretion system to inject effector proteins into a host cell. Recently, a putative Toxic GTPase Activating Protein (ToxGAP) called VopE was identified as a T3SS substrate and virulence factor that affected host mitochondrial dynamics and immune response. However, biophysical and structural characterization has been absent. Here, we describe solution NMR structure of the putative GAP domain (73-204) of VopE. Using SEC-SAXS and RDC data, we restrained the MD process to efficiently determine the overall fold and improve the quality of the output calculated structures. Comparing the structure of VopE with other ToxGAP's revealed a similar overall fold with several features unique to VopE. Specifically, the "Bulge 1", α 1 helix, and noteworthy "backside linker" elements on the N-terminus are dissimilar to the other ToxGAP's. By using NMR relaxation dispersion experiments, we demonstrate that these regions undergo motions on a >6 s⁻¹ timescale. Based on the disposition of these mobile regions relative to the putative catalytic arginine residue, we hypothesize the protein may undergo structural changes to bind cognate GTPases.

Keywords: GTP hydrolysis, Vibrio Cholerae, mitochondrial dynamics, small-angle x-ray scattering, relaxation dispersion, helical bundle, catalytic arginine finger, T3SS secretion system, YopE, ExoS

INTRODUCTION

Vibrio cholera are gram negative, curved-shaped bacteria that globally cause approximately 100,000 deaths per year. To evade host organism immune response, bacteria use Type III Secretion Systems (T3SS). Upon infection, T3SS components inject effector proteins into the host cell, which in turn disrupt the "normal" physiological responses. First described to disrupt the actin cytoskeleton, these effector proteins have also been shown to affect gene transcription, cell cycle progression, and organelle trafficking. As mitochondria play a role in all these processes, it is not surprising that they are targets of bacterial effector proteins as well. However, for the dozens to hundreds of bacterial effectors that have been characterized, only a couple have been shown to modulate mitochondrial dynamics. Section 2.

GTPases are among the most critical class of signaling proteins in the cell. While small GTPases are very diverse, the most well-studied is Ras. Ras is considered a "switch-like" GTPase because it cycles between two "locked" (tightly bound, low-exchanging) states: GTP- and GDP-bound. In its GTP-bound state, Ras can interact with a multitude of binding partners and lead to activation of signaling cascades. ¹⁰ In its GDP-bound state, Ras binds weaker to its partner proteins to downregulate signaling and be an "off state". Because hydrolysis and exchange of guanosine nucleotides is relatively slow, proteins called "GTPase-Activation Proteins" (GAP's) accelerate hydrolysis by orders of magnitude. ¹³ In this way, they modulate activation of signaling cascades. Structurally, the first discovered GAP's contained a so-called "catalytic arginine fingers". A complex of Ras and RasGAP showed the GAP arginine residue protruded into the GTPase active site. ¹⁴ The side chain guanidino group coordinates the GTP phosphates to promote the hydrolysis from GTP to GDP*phosphate (Figure S1). ¹⁵ While there are

exceptions,¹⁶ this "arginine finger" appears to be the most frequent mechanism of GAP-mediated GTP hydrolysis in mammals.¹⁷⁻¹⁹ Furthermore, there is also frequently a threonine residue which binds to the ribose of the GTP to better align the catalytic arginine, though its presence or absence has not been well described in the literature.

One class of effector proteins is named Toxic GTPase-Activating Proteins (ToxGAP) from bacteria. Host cell GTPases have been implicated in hundreds of cellular functions. Therefore, activation or altering the activity of GTPases has been a common strategy employed by bacterial effector proteins to avoid host cell immune responses. Rho GTPases were first identified as targets of these ToxGAP's based on the altered cytoskeleton phenotypes during infection. Since initial work, others have shown Arf''s, Rab's, and other families of GTPases are similarly targeted by different ToxGAP's. Interestingly, GAP's such as VirA show little specificity and *in vitro* activate a number of host cell GTPases, though it is not known how specific most ToxGAP's are. Catalytic arginine residues are required for activity in three separate classes of ToxGAP's. The structures of ToxGAP's themselves are quite varied, with some being simple alpha helical bundles to larger ones more similar to RasGAP25 to α/β ArfGAP-like27 to even larger TBC-like domains. Several human GAP's share structural homology with toxin ones, though four-helix bundles have only been reported from bacteria. However, it is not known if/how the fold of the protein affects activity or specificity.

In characterizing T3SS's in *V. cholerae*, Alam et al. discovered an effector protein which they and others named *Vibrio* outer protein E (VopE).²⁸ Though its molecular function was initially unknown, Tam et al. showed it translocated into the host cell.²⁹ Additionally, knockout of VopE caused reduced severity of symptoms in a rabbit *V. cholerae* infection model.³⁰ Adding

more mechanistic details, Suzuki et al. reported that VopE was a ToxGAP targeted to mitochondrial GTPases.³¹ VopE's domain architecture of VopE includes three domains: a mitochondrial targeting sequence (MTS), an unknown region, and a putative GAP domain (Figure 1a). Even a single point mutation in the MTS has been shown to affect mitochondrial localization.³¹ And a point mutation to the putative catalytic arginine has been shown to reduce mitochondrial clustering effects in the context of *V. cholerae* infection. Suzuki et al. proposed the Miro1/2 GTPases as the target of VopE, based on a relatively modest increase in relative hydrolysis activity.

Our work focuses on the putative activating domain, as it has been demonstrated to be required for aberrant mitochondrial dynamics phenotypes. Despite the excitement of the initial cellular studies, biophysical and structural characterization of the protein has been lacking. Additionally, the closest homolog of VopE, YopE, is only 34% identical to VopE (Figure S2) and when comparing all known ToxGAP's with structures (three others), the identity drops to 4.9%. This overall low identity precludes detailed structural studies by computational modeling.³² To generate a high-resolution structure of VopE, we used integrative Small Angle X-ray Scattering (SAXS) and NMR data to calculate the NMR structural ensemble. We find especially large differences in the α 1, α 2, and "backside linker" elements. Using relaxation dispersion experiments, we also find these elements undergo conformational changes on a relatively fast timescale. Given these unique elements and their motions, we hypothesize on the function of VopE in GTPase binding and catalysis.

RESULTS

Scattering experiments show the VopE GAP domain is monomeric and elongated

The largest soluble fragment, corresponding to amino acids 73-204, will hereafter be referred to as "VopE". We expressed and purified VopE from *E. coli*. As hetero- and homooligomeric state regulates the function of many GTPases, like SRP,³³ dynamin,³⁴ and Ras,³⁵ we initially performed size-exclusion chromatography coupled with multi-angle light scattering (SEC-MALS) on VopE to determine its oligomeric state in solution. Two protein standards, bovine serum albumin (BSA) and carbonic anhydrase (CA), eluted at the expected volume with the properly estimated monomeric molecular weights (Figure 2a). The MALS-calculated molecular weight of VopE was only 7% different than the theoretical molecular weight of this construct, indicating a monomeric state. VopE also elutes significantly before CA, indicating a larger radius of hydration (R(h)) than CA despite its smaller molecular weight (30 kDa vs. 14.9 kDa). The difference in radii of hydration was confirmed by quasi-electric light scattering (QELS) (Table S1).

To obtain more structural information, we then performed size exclusion chromatography coupled with small-angle x-ray scattering (SEC-SAXS) (Figure 2b). Guinier and P(r) plots were consistent with an elongated protein (Figure 2c, 2d). And the Kratky plot is consistent with that of a primarily well-folded protein (Figure 2e). Facilitated by the scattering data, we employed higher resolution methods to investigate the structure of VopE.

NMR structures obtained using SAXS and RDC restraints show an elongated, seven helix bundle

we then calculated a structural ensemble of VopE using NMR spectroscopy. Briefly, 2D and 3D NMR spectra were used to assign the ¹H, ¹³C, and ¹⁵N resonances from the backbone and sidechains of recombinant VopE (Figure S3); the chemical shift assignment completeness for all atoms was 81%. The resonance assignments, SAXS scattering data, residual dipolar couplings (RDC's), and 3D NOESY spectra were utilized for Xplor-NIH-based structure calculation through the PONDEROSA-C/S suite,³⁶ in an iterative process of structure calculation and constraint validation. Since the work of Grishaev et al.,³⁷ a couple of software packages have been developed to incorporate SAXS scattering data.³⁸ However, of the 12,882 solution NMR structures in the PDB, only five of them contain both SAXS and RDC restraints for use in NMR structure calculations. The use of our SAXS data allowed the structures to more efficiently converge to a similar, bundled shape without the need for significant manual input. To validate our presumed primarily alpha helical structure, we also collected RDC data. The calculated RDC values agreed well with our experimental values in the lowest energy conformer (Figure S4).

Our method calculated the top 100 most energetically stable VopE conformers representing the 3D structure, from which the NMR structures and statistics of the top 20 are shown in Figure 3a and Table 1, respectively. The final structure calculation had no constraint violations among the top 20 conformers and backbone phi/psi angles in these structures were in favored regions of the Ramachandran plot for 96.2% of all ordered residues. NMR data were deposited in the BioMagResBank³⁹ (BMRB ID 30756) and the structural coordinates and

restraints were deposited in the Protein Data Bank⁴⁰ (PDB ID 6X6N). The secondary structure overlaid with the sequence is shown in Figure S5.

SEC-SAXS ab initio reconstructions exhibited a "lightbulb" shape, consistent with our NMR structure calculations (Figure 3b). Also consistent with our hydrodynamic and scattering data, the protein has an unfolded N-terminus (73-83) and is otherwise comprised of an elongated, alpha helical bundle. The secondary structural elements are shown as cylinders in Figure 4a and labeled according to the ExoS ToxGAP convention.⁴¹ The secondary structure of our construct is 62% alpha helical, 2% beta strand, and 36% other. The protein contains seven alpha helices (labeled α 1-7), with most helices aligned "vertically". The α 1, α 3, α 4, and α 7 helices run antiparallel to the α 2, α 5, and α 6 helices in an up-and-down manner with the N- and C-termini on the same side of the molecule.

By referencing the structures of two similar ToxGAP proteins crystallized with their cognate GTPase, 24,42 and because of previous mutagenesis studies, 31 we are able to predict the active site residues. Similar to other ToxGAP's, VopE has two protruding "bulges" between alpha helical elements. VopE's putative catalytic "arginine finger" (Arg125) in the top of α 3, as with all other ToxGAP's with published structures. The three cysteine residues were all reduced under our conditions and spread throughout the protein. When viewing the putative active site surface, there does not appear to be a charge bias, despite the relatively low theoretical pl of 5.7 (Figure S6). There is also no apparent localization of hydrophobic residues on this surface.

Comparison with other ToxGAP domains reveals similar overall fold with structural differences in the of $\alpha 1$, $\alpha 1/2$ linker, $\alpha 2$, and Bulge 1 elements

Structures of three other ToxGAP's which are alpha helical bundles have been published. $^{26,41.42}$ These structures are very similar to each other in overall fold and location of their catalytic residues (Figure S7). Like VopE, each positions its catalytic arginine finger in the middle of α 3. Aside from the helical content, there also appears to be two slightly less-structured elements in VopE that correspond to the so-called "Bulge 1 and Bulge 2" in ExoS, YopE, and SptP. Würtele et al. demonstrated that these bulge regions had the greatest reduction in B-factors between the unbound and GTPase-bound ExoS domain, which they attribute to a loss of flexibility upon binding. 41

When observing the ToxGAP-conserved residues compared to our structure, we find the core hydrophobic residues are all similarly placed amongst each other, also as expected for folding and proper placement of helices. Aside from the putative catalytic Arg125 residue, the only other residue that is conserved on the active site interface is Thr164 (Figure 4b). In the ExoS/Rac co-crystal structure²⁴ as well as the SptP/Rac co-crystal structure,⁴² and more broadly in the less-related RasGAP,¹⁴ the threonine side chain hydroxyl is making a hydrogen bond with the 3' hydroxyl of the ribose in GTP. This interaction is likely to be conserved in VopE given that a threonine residue is conserved at this location among all ToxGAP's, and its disposition, and solvent accessibility in our structure is similar.

To take a more detailed look at the differences between VopE and other ToxGAP's, we overlaid of VopE and YopE (Figure 4c). The overall fold of the proteins is similar, with several distinct differences. First, the angles and position of α 3 and α 4 are particularly displaced

between the structures. This leads to a relatively high overall RMSD between the structures (4.83 Å) despite their relatively similar folds. Additionally, there are two regions in VopE which we predict may influence the active site dynamics. Both Bulge 1 and the loop between α 1 and α 2 in VopE are significantly divergent from other ToxGAP's (Figure 4d).

The linker between $\alpha 1$ and $\alpha 2$ contains significantly less secondary structure than its orthologs. In the ortholog ExoS, the alpha helical nature of this region is also conserved in both the crystal and NMR structures (PDB ID: 1HE9, 1R4T), ruling out the possibility of a secondary structure change due to crystallization conditions. Because the sequences in this region are quite dissimilar, it is not surprising to observe these structural differences. Finally, while in the ExoS/Rac1 structure $\alpha 1$ contributes to a hydrophobic interaction with Rac1, VopE's $\alpha 1$ is significantly displaced. These distinctive regions adjacent to the putative active site led us to study the dynamics of these regions further.

Relaxation dispersion experiments show mobility in the unique N-terminal elements which may exhibit effects on binding to cognate GTPases

To investigate the structural mobility of these regions of VopE, we used NMR for further studies. Slow timescale (microsecond-to-millisecond) motions in the structure of biomolecules can be detected using constant-time relaxation-compensated CPMG experiments. We calculated the chemical and conformational exchange contribution to transverse relaxation (R_{ex}) after fitting the dispersion curves for effective transverse relaxation rate (R_2^{eff}) against CPMG frequency (v_{cpmg}) (Figure S8). We then plotted transverse relaxation as a function of residue number (Figure 5a) The results revealed that the structure of VopE-GAP exhibits

flexibility in $\alpha 1$, the backside linker, Bulge 1, and the short $\alpha 2$ between these loops (Figure 5b). It is plausible to think that the motions of Bulge 1 near the putative active site could be linked to the other mobile adjacent regions. The high R_{ex} values (> 6 sec⁻¹) of residues in this region suggests that their backbone could exchange between multiple conformations.

Because there is no VopE-GTPase complex structure, we analyzed the co-crystal structure of P. aeruginosa ExoS GAP and H. sapiens Rac GTPase with GDP-AIF₃ (PDB ID 1HE1)²⁴ to gain insight into the differences between unbound and bound ToxGAP domain conformations. Upon the binding with a Rac protein, the poorly structured backside linker and Bulge regions of the ExoS GAP domain become more structured, placing its active site residues (corresponding to R125 and T164 for VopE) closer to the substrate (Figure 5c). Bulge 1 binds to the cognate GTPase in both ExoS/Rac1 and SptP/Rac1 (PDB ID: 1G4U). In VopE, α 1 (residues Phe93, Gln97, Ile110) and the structurally adjacent Gly201 are also notably more mobile, and compared to the other ToxGAP structures, displaced significantly further away from a putative binding partner. Additionally, the relatively mobile $\alpha 2$ in VopE forms an apparently stable, and more extensive alpha helix than in the structures of ExoS (crystal), ExoS (NMR), YopE (crystal), and SptP (crystal) structures. In the co-crystal structure of ExoS and Rac, α 1 of ExoS interacts with the GTPase via hydrophobic interactions. In VopE, the analogous helix is significantly displaced and partially disordered. We hypothesize that α1 and the disordered N-terminus may undergo conformational change upon binding to a GTPase. Therefore, our data could imply that the conformational exchange of the VopE GAP-domain in its $\alpha 1$, backside linker, $\alpha 2$, and Bulge 1 in these unique regions could be important for proper assembly and/or activity of the catalytic complex. We speculate these loops may accommodate binding to its cognate GTPase. Given the

regions putative function in substrate binding, it is plausible to hypothesize it could proceed through an induced fit mechanism.

DISCUSSION

We have calculated the NMR structures of the ToxGAP domain of VopE and investigated its dynamics via relaxation dispersion experiments. Surprisingly, we find that the N-terminal $\alpha 1$, backside linker, $\alpha 2$, and Bulge 1 elements differ greatly from other homologous ToxGAP's. Based on these differences, we hypothesize that either VopE may undergo a conformational change upon binding to substrate GTPase(s), or that the VopE GAP-GTPase complex differs from those previously described in the literature. Without additional structural studies with its cognate GTPase, these potential conformational changes remain untested.

The most obvious open question is how VopE interacts with its binding partner(s). The work of Suzuki et al. is limited in that they only test activation of Miro by VopE. However, it is probable that VopE activates Miro in the context of the cell when both are localized to the Outer Mitochondrial Membrane (OMM). However, as the GAP's VirA²³ and Rabenosyn-5⁴⁴ show broad specificity to 3-6 GTPases, it is possible VopE exhibits similar effects upon GTPases like Mitofusin1/2,⁴⁵ Dynamin,⁴⁶ Miro1/2,⁴⁷ Rab24⁴⁸ and Rab32.⁴⁹ Additionally, several post-translational modifications have been established for HsMiro1/2^{50,51} which may affect its interaction with binding partners during infection *in vivo*. It has not yet been determined if VopE activates any other GTPase, and if so, the conformational changes that VopE does or does not undergo. Unfortunately, VopE has no sequence identity with any mammalian protein. It will

also be interesting to see whether other mammalian proteins, if any, could activate Miro's GTPase activity.

MATERIALS AND METHODS

Reagents and Media

 13 C glucose (99%, Cambridge Isotope Laboratories) and 15 N ammonium sulfate (99%, Cambridge Isotope Laboratories) were used without further purification. TPM media was comprised of 20 g tryptone, 15 g yeast extract, 8 g NaCl, 2 g dibasic sodium phosphate, and 1 g monobasic sodium phosphate per 1 L of media. M9 minimal media was comprised of 10 mL of MEM vitamin solution (Sigma Aldrich), 500 μL of 2 M MgCl₂, 100 μL of 1 M CaCl₂, 2 g of glucose and 1 g of ammonium sulfate per 1 L of media. Carbonic anhydrase and chicken egg albumin (ovalbumin), were commercially available (Sigma Aldrich), dissolved in the appropriate buffer and used without further purification.

Cloning and Sequencing

Experiments were performed at Northwestern University in the Department of Cell & Developmental Biology (Chicago, IL). VopE cDNA was provided by the Mekelanos Lab (Cambridge, MA). Fragments were PCR amplified using CloneAmp HiFi PCR Premix (Clonetech) using the protocol supplied by the manufacturer. Fragments were subcloned into pET-28b vectors (Novagen) via Nco1 and Xho1 restriction sites using In-Fusion ligation-independent cloning (Clonetech). Site-directed mutagenesis (Quikchange, Agilent) was employed to insert an N-terminal PreScission protease cleavage site in VopE. Plasmids were amplified and purified

using commercial protocols (Qiagen) as directed. DNA sequences were verified by Sanger sequencing (Northwestern University NUSeq Core).

Secondary Structure Prediction

Our protocol was identical to the work of Agarwal et al.⁵² The full sequence of *V.cholera* VopE (Uniprot ID: A0A0H7DTI2) was input into 10 different secondary structure prediction servers. By using many different algorithms and servers, we aimed to reduce the bias from any one method. Peng et al.⁵³ and Fan et al.⁵⁴ suggest multiple servers complement each other and allow for more accurate predictions. The 10 servers used were PSIPRED,⁵⁵ IUPRED,⁵⁶ PONDR,⁵⁷ DisEMBL,⁵⁸ s2D,⁵⁹ ESpritz,⁶⁰ PROFsec,⁶¹ MFD2p,⁵⁸ DISCoP,⁵⁴ and YASPIN.⁶² We used a cutoff of >50% likelihood within each algorithm to classify a residue as "disordered." The results of each server were converted to a binary output of "folded/unknown" or "disordered" (0 or 1 respectively). The scores were summed and plotted as a function of amino acid number.

Sequence Alignments

VopE (A0A0H7DTI2), YopE (P31493), ExoS (Q51449), and SptP (P74873) sequences were aligned via UNIPROT⁶³ using BLAST.⁶⁴

VopE Expression and Protein Purification

Experiments were performed at Northwestern University in the Department of Cell & Developmental Biology (Chicago, IL). Cells were grown, induced, lysed, and clarified identically to HsMiro1/2 constructs previously described.⁵¹ All recombinant proteins were expressed using

E. coli BL21 RP (DE3) strain (Novagen). After inoculating 2 L of TPM media in a 6 L Erlenmeyer flask (VWR) with 2 mL of overnight starter culture, the cells were grown with shaking at 200 rpm for approximately 5 hours at 37°C to OD₆₀₀=0.45. The temperature was then lowered to 16°C for 1 hour and then cells were induced at OD₆₀₀=0.90 with 0.125 mM IPTG for approximately 18 hours overnight. Expression conditions were based on a "standard lab protocol" and did not require optimization for reasonably high yields. The cells were resuspended in 50 mM HEPES*HCl (pH 8.0), 500 mM NaCl, 1 mM MgCl₂, 0.5 mM TCEP, and 5% sucrose (w/v) before flash freezing in liquid nitrogen. The cell pastes were stored at -80°C for less than 3 months before lysis and purification. Cells were thawed at 37°C and all lysis and purification steps were performed at 4°C. The cell pastes were sonicated for 4x45 seconds at 100% amplitude using a Q125 Sonicator (QSonica) before clarifying at 35,000 rpm for 45 min. The soluble lysate from 8 L of culture was incubated with 10 mL of 50% Co²⁺ TALON® bead slurry (Clonetech).

The beads were washed with 10x10 mL of wash buffer (25 mM HEPES*HCl pH 7.4, 500 mM NaCl, 0.25 mM TCEP). Tag cleavage was initially performed in solution with success, but onbead cleavage was more time-effective while being equally as efficient. The tag was cleaved off while the protein was bound to the beads by incubation with 200 units of Prescission Protease (GE Healthcare) at 22°C with rotation for 1 hour. The protein and protease eluted off the beads, which were washed with approximately 5x3 mL of wash buffer. The protein was concentrated to approximately 2.5 mL using 3 kDa MWCO spin concentrators (Amicon) before injection over a 16/60 Superdex 75 (S75) size exclusion column (GE Healthcare) in S75 Buffer (10 mM HEPES pH 7.4, 150 mM NaCl, 0.5 mM TCEP). Pure fractions were pooled and concentrated to

approximately 10 mg/mL before flash freezing in liquid nitrogen and storage at -80°C.

Approximate final yields were 20 mg of pure protein per 1 L of culture. Unlabeled protein from two separate preparations was used for all SAXS experiments. Protein concentration was calculated using the theoretical extinction coefficient⁶⁵ of all tryptophan, tyrosine, and reduced cysteine residues in our construct at 280 nm (4470 M⁻¹ cm⁻¹) on a NanoDrop 1000 spectrophotometer (ThermoFischer). Our recombinantly expressed and purified protein was >95% pure by SEC-MALS Abs280 and >95% pure with full tag cleavage via Coomassie-stained SDS-PAGE (Figure S9), validating our purification methods.

VopE Expression for Isotopic Labeling

Experiments were performed at Northwestern University in the Department of Cell & Developmental Biology (Chicago, IL). For ¹³C and/or ¹⁵N labeling of VopE, 500 mL cultures of M9 minimal media (5.64 g 5x M9 minimal salts, 10 mL 100x MEM Vitamins, 1 g D-glucose, 0.5 g ammonium sulfate, 50 μL 1M CaCl₂, 500 μL 1M MgCl₂) were used with ¹³C labeled D-glucose and/or ¹⁵N labeled ammonium sulfate (Cambridge Isotope Laboratories). Expression was slightly improved in autoinduction media but was not as cost efficient. The final antibiotic concentration was increased to 0.1 mg/mL of kanamycin and .068 mg/mL chloramphenicol to reduce plasmid loss and poor yields. Cultures were grown in 2.5 L Ultra Yield[™] flasks (Thomson Instrument Company) for increased aeration. 500 mL cultures were inoculated with 2 mL of overnight preculture cells. The cultures were grown in darkness at 37°C with shaking at 250 rpm until an OD₆₀₀ of 0.4, when the temperature was lowered to 22°C for 1 hour. The cells were induced at an OD₆₀₀ of 0.6 with 1mM IPTG for approximately 15 hours. Cell pelleting, lysis and

protein purification were identical to that of the unlabeled protein. Approximate final yields were 10 mg of pure protein per 1 L of culture. Protein purity was ensured through SEC and SDS-PAGE analyses. Protein from a first 2L preparation was used in all NMR residue assignments, RDC calculations, and structural calculations. Protein from a second, 2L preparation was used for relaxation/dispersion experiments.

SEC-MALS

Experiments were performed at Northwestern University in the Keck Biophysics Facility (Evanston, IL). Solution SEC-MALS experiments were conducted using a 1200 LC HPLC system (Agilent Technologies, Santa Clara, CA) equipped with 18-angle MALS light scattering detectors (Wyatt Dawn Heleos II), a refractive index detector (Optilab T-rEX), a quasi-elastic (dynamic) light scattering (QELS) detector (WyattQELS) and ASTRA analysis software (Wyatt Technology Europe GmbH). Proteins were first buffer exchanged into SEC-MALS buffer (10 mM HEPES at pH 7.4, 150 mM NaCl, 0.5 mM TCEP) using a Superdex 75 (S75) 10/300 GL column (GE Healthcare), spin concentrated to 25.1 mg/mL and cleared of aggregates by ultracentrifugation (100,000 rpm for 10 mins). A total of 350 μL of VopE was injected and run on the S75 column at a flow rate of 0.5 mL/min in SEC-MALS buffer at 10°C. All tubing was lined with 4°C cold packs to prevent sample heating and unfolding. Bovine serum albumin (BSA, Sigma-Aldrich) and beta amylase (Sigma Aldrich) at approximately 2 mg/mL each were mixed and run as molecular weight controls to experimentally determine a dn/dc value (0.187 mL/g) under our conditions.

SEC-SAXS

Measurements of x-ray scattering data were carried out at the APS BioCAT beamline (Sector 18-ID) of Argonne National Laboratory, as described by Mathew et al. 66 The 12-keV Xray beam ($\lambda = 1.033$ Å) was focused on a 1.5-mm quartz capillary sample cell with 10 μ m walls. The scattering, in the momentum transfer range, $q = 0.0038-0.4 \text{ Å}^{-1}$, was collected on a Dectris Pilatus 3X 1M detector approximately 1.5 m downstream of the sample position. All instrumentation and experiments were performed at 25°C. VopE 73-204 in VopE buffer (10 mM HEPES*HCl pH 7.4, 150 mM NaCl, 0.5 mM TCEP) was fed into the X-ray beam after passing through a Superdex 75 (S75) 10/300 GL or Superdex 200 (S200) Increase 10/300 GL column (GE Healthcare) onto which 300 - 500 μl was loaded at 19.5 – 31.8 mg/ml. A flow rate of 0.75 mL/min was used for all samples. The delay between protein emerging from the SEC column and its arrival at the beam position was approximately 1 min. SAXS exposures with a length of 1.0 sec were collected every 3.0 sec during the gel filtration chromatography run. Scattering data was radially averaged, processed, scaled, averaged, and analyzed using PrimusQT.³⁴ Exposures before and after sample elution were averaged and used as buffer background. Pair distribution functions, P(R), of the scattering centers were computed from the scattering curves using GNOM.³⁵ The radius of gyration was not concentration-dependent and was extremely similar throughout the elution profile. Inspection of the scattering and Guinier plots show the data is of high quality and the linearity in this region confirms the Rg value can be used in further analyses. The molecular weight was calculated by multiplying the Porod volume by 0.625, the average ratio between molecular mass and Porod volume for 53 proteins examined.³⁶ Also of note, two distinct x-ray datasets collected on two distinct protein

preparations had nearly identical Rg values (±5%), further validating our prep-to-prep protein and SAXS system reproducibility. Electron density reconstruction was made by generating 10 reconstructions with DAMMIF, averaged with DAMAVER, and refined with DAMMIN. Final statistics are reported in Table 1. Our data has been submitted to the SASBDB⁶⁷ under accession code SASDJV3.

Crystallization Trials

Crystallization trials were performed at the Northwestern Structural Biology Facility (Chicago, IL). A total of 23 different constructs were subjected to crystallization trials after parallel purification. Proteins at 5-20 mg/mL was mixed in a 1:1 ratio with precipitant. MCSG1-4 screens were employed.⁶⁸ No well-diffracting, 3D crystals were ever obtained, and we proceeded with structural experiments using NMR.

NMR Sample Preparation

During preliminary optimization experiments, we observed the protein was prone to degradation and precipitation at higher temperatures (37°C) and lower pH (5.0) over the course of days, as judged by visible inspection and HSQC spectra. 3D NMR data were collected with 1.05 mM 13 C/ 15 N VopE in NMR Buffer (10 mM HEPES*HCl pH 6.0, 150 mM NaCl, 0.5 mM TCEP) before being diluted in approximately 10% (v/v) D_2 O (Sigma-Aldrich). Samples were passed through a 0.22 μ m filter before being transferred to 5-mm susceptibility-matched Shigemi NMR tubes (Shigemi). The total sample volume was approximately 300 μ L and final protein concentration was approximately 960 μ M. 1 H/ 15 N 2D HSQC experiments were performed

before and after 3D data collection. Spectra were overlaid to ensure sample homogeneity and stability over the course of the experiment.

NMR Data Collection and Processing

All experiments were performed at the University of Wisconsin-Madison in the NMRFAM facility (Madison, WI). Data were collected on a Varian VNMRS spectrometer (Agilent Technologies, Santa Clara, CA) operating at 600 MHz (¹H), equipped with a cryogenic triple resonance probe using VnmrJ 4.2. The temperature of the samples was regulated at 25.0°C for all experiments. All samples were equilibrated with the probe for approximately 15 minutes before data collection.

2D ¹H, ¹⁵N-HSQC and 3D HNCACB, 3D CBCA(CO)NH, and 3D HNCO spectra were recorded to enable backbone assignments. 2D constant-time ¹H, ¹³C-HSQC optimized for the ¹³C aliphatic region and 3D C(CO)NH, 3D HBHA(CO)NH, 3D H(C)CH-COSY and 3D H(C)CH-TOCSY spectra were acquired to enable assignment of the remaining ¹H and ¹³C resonances in the aliphatic spectral region. Aromatic data was collected on a second ¹³C/¹⁵N protein sample from the same protein preparation as the initial sample. 2D constant-time ¹H, ¹³C-HSQC optimized for the ¹³C aromatic region and 2D (HB)CB(CGCD)HD, 2D (HB)CB(CGCDCE)HE and 3D H(C)CH-TOCSY spectra were acquired to enable assignment of the ¹H and ¹³C resonances from the aromatic rings. Finally, for structure calculation, a 3D NOESY ¹⁵N-HSQC spectrum and two 3D NOESY ¹³C-HSQC spectra optimized for aliphatic and aromatic ¹³C resonances, respectively, were recorded using a 100 ms mixing time.

All spectra were processed using NMRPipe.⁶⁹ All 3D spectra were recorded using non-uniform sampling (NUS) with a sampling rate of ~40%. A Poisson-gap sampling⁷⁰ schedule was used for the NUS data acquisition and the SMILE plug-in⁷¹ in NMRPipe was used for spectral reconstruction.

Residual dipolar coupling (RDC) NMR experiments were carried out at 25°C using a Bruker Avance III (Bruker) spectrometer operating at 750 MHz equipped with a 5 mm TCI cryoprobe. RDCs were extracted from 2D ARTSY (72) spectra at 25°C using a 1 mM ¹³C/¹⁵N labeled VopE sample in 10 mM HEPES, pH 6.0, 150 mM NaCl, 0.5 mM TCEP, 10% (v/v) D2O sample for the isotropic state and a similar sample containing 0.4 mM C/N VopE supplemented with 12 mg/ml filamentous Pf1 phage (ASLA Biotech, Riga, Latvia) for the anisotropic state.

NMR Relaxation Dispersion Data Collection

Relaxation dispersion experiments were recorded on an Avance III Bruker spectrometer operating at 600MHz (1 H) and equipped with a triple resonance cryogenic probe. The temperature of the sample was regulated at 298 K for the duration of the data collection. The relaxation experiments were acquired as interleaved 2D 1 H- 15 N HSQC spectra with the total CPMG delay set to 40ms. In addition to the reference experiment, recorded without the relaxation period, the number of 15 N 180 pulses during the CPMG delay was adjusted to acquire 14 unique v_{CPMG} values: 50, 100, 150, 200, 250, 300, 350, 400, 500, 600, 700, 800, 900, 1000 Hz. Two v_{CPMG} values (100 and 400Hz) were recorded twice to estimate error in the data. The recycle delay between scans was set to 3.0sec. The offset and the spectral width were set to 4.76 and 16.0 ppm for the 1 H t₂ dimension and to 114.0 and 29.9 ppm for the 15 N t₁ dimension.

A total of 1024 and 128 complex points were acquired for the ¹H and ¹⁵N dimensions, respectively. 32 scans were accumulated for each FID, resulting in a total recording time of 3 days and 12 hours. 2D ¹H-¹⁵N HSQC spectra were recorded immediately before and after the relaxation dispersion experiment to ensure that the sample was stable for the duration of the long relaxation experiment. The spectra were processed using NMRPipe and inspected using NMRFAM-Sparky.

NMR Assignments

Software packages were provided by NMR Box. ⁷³ For backbone assignments, the 2D ¹H, ¹⁵N-HSQC and 3D HNCACB, 3D CBCA(CO)NH and 3D HNCO spectra were analyzed in NMRFAM-SPARKY (74). The program APES⁷⁵ was used for automated peak picking. After manual inspection, the peak lists from 3D and 2D spectra were submitted to the I-PINE web server (http://i-pine.nmrfam.wisc.edu)⁷⁶ for automated backbone assignments using PINE-SPARKY.2 automation plugin (two-letter-code ep)⁷⁷ in NMRFAM-SPARKY. These automated assignments were then verified and extended by hand using the tools available in NMRFM-SPARKY. The final backbone chemical shifts were then analyzed to evaluate the structure of VopE in solution by running PECAN. ⁷⁸ After complete backbone assignments, we employed *predict-and-confirm* strategy using *transfer-and-simulate* tool available in NMRFAM-SPARKY for aliphatic sidechain assignments³⁸ on 2D aliphatic ¹H, ¹³C-HSQC, 3D HBHA(CO)NH, (H)C(CO)NH, H(CCO)NH, H(C)CH-COSY and H(C)CH-TOCSY. Subsequently, we also used *predict-and-confirm* strategy to complete aromatic sidechain assignments on 2D aromatic ¹H, ¹³C-HSQC, CBHD, CBHDHE and 3D aromatic H(C)CH-TOCSY. PACSY⁷⁹ was used to simulate peak locations for this

Page 24 of 53

semi-automatic assignment routine. All assigned chemical shifts have been deposited in the BMRB³⁹ under accession code 30756.

NMR Structure Calculations

An NMR-STAR 3.1 chemical shift file was generated by a plugin of NMRFAM-SPARKY and used as input to the PONDEROSA C/S software package³⁶ with the Xplor-NIH calculation option⁸⁰ along with the raw 3D ¹⁵N-edited NOESY and ¹³C-edited aliphatic and aromatic NOESY spectra. AUDANA automation option⁸¹ was selected to automate NOESY analysis and dihedral angle prediction. As a result, NOE-derived distance constraints were obtained by the AUDANA algorithm and backbone chemical shift-derived angle constraints were obtained by TALOS-N. Tolerances were set to 0.025, 0.35, and 0.35 ppm for ¹H, ¹³C, and ¹⁵N, respectively. The PONDEROSA-Client program includes an automatic NOE cross peak detection module connected to a visual noise level selector in NMRFAM-SPARKY.⁸² Structure calculations were tested with both AUDANA⁸¹ and CYANA.⁸³ We used secondary structure probabilities from PECAN⁷⁸ as whitelist restraints for the efficient NOE assignment. The PONDEROSA-Client program then submitted the structure calculation job to the PONDEROSA web server. Subsequently, we used the "Distance Constraint Validator" and "Angle Constraint Validator" of the Ponderosa Analyzer to validate the constraints. Semi-automated calculations were performed by manually inspecting using the "validation" tools in Ponderosa Analyzer. Constraints were visualized with PyMOL, and the corresponding NOE cross peaks were visualized synchronously with NMRFAM-SPARKY. Inspired by previous work combining SAXS and NMR data, 37,84,85 we "refined" the accuracy of our NMR solution structures using our

experimentally obtained SAXS data. After constraints were verified, they were submitted to the PONDEROSA web server using the Constraints-Only X option, which utilized Xplor-NIH to carry out high-temperature dynamics, simulated annealing, and low-temperature dynamics. Resonance assignments, 3D NOESY, RDC and SAXS data were used as inputs initially. After a few iterations of structure calculation using the "Constraints Only-X" option in PONDEROSA-C/S, the final conformers representing the hybrid solution structure were determined by using refined constraints and SAXS curve data with the "implicit water refinement calculation(x2)" option in Ponderosa Client program, which calculates 200 conformers and selects the 20 best on the basis of the EEFX potential energy term. Once the protein appeared to converge towards a final structure, we used the previous coordinate files as inputs as well. A total of 2492 NOE restraints (1482, 617, and 266 constraints for short-, medium-, and long-range, respectively) and 200 dihedral angle constraints (101 φ angles and 99 ψ angles) were used for structure calculation (Table 1). We used PSVS suites⁸⁶ to validate the calculated structures and correct overconstrained residues. The agreement between the experimental RDCs measurements and RDC values back calculated from the structure served to validate the structure. Structural NMR statistics for the 20 most energetically stable VopE conformers are summarized in Table 1. Coordinates were deposited to the PDB under the accession code 6X6N.

NMR Relaxation Dispersion Analysis

Effective transverse relaxation rate (R_2^{eff}) at each CPMG frequency (v_{cpmg}) were calculated using:

$$R_2^{eff} = \frac{1}{T_{CPMG}} ln \frac{I(0)}{I(v_{cpmg})}$$

 T_{CPMG} is the constant CPMG time, $I(v_{cpmg})$ is the peak intensity at each v_{cpmg} , and I(0) is the peak intensity at $v_{cpmg} = 0$. For the CPMG experiment of VopE-GAP, T_{CPMG} was set to 40 ms. Dispersion curves for R_2^{eff} against CPMG frequency were fitted using scipy.optimize.curve_fit (https://docs.scipy.org/doc/scipy/reference/generated/scipy.optimize.curve_fit.html). The curves were fitted by one of exchange models: model 1 (No exchange), model 2 (fast exchange), and model 3 (slow exchange). After fitting by all models, the model with the smallest deviations ($\sum_n [R_2^{eff}(n, \text{fitted}) - R_2^{eff}(n, \text{observed})]^2$) was selected for each residue. For model 1 (no exchange), the fitting equation was:

$$R_2^{eff}(\mathsf{v}_{cpmg}) = R_2^{eff}(\mathsf{v}_{cpmg} \to \infty)$$

 $R_2^{eff}(v_{cpmg})$ is the R_2^{eff} value calculated for each v_{cpmg} and $R_2^{eff}(v_{cpmg} \rightarrow \infty)$ is the R_2^{eff} value at infinite v_{cpmg} .

Model 2 refers to the fast-limiting ($k_{ex} \gg \Delta \omega$) exchange between two chemical/conformational states, A and B. k_{ex} is the rate constant of the exchange reaction and $\Delta \omega$ is the chemical shift difference upon the exchange. For model 2, the Luz-Meiboom equation was used for fitting k_{ex} , Φ (= P_A P_B $\Delta \omega^2$), and $R_2^{eff}(v_{cpmg} \rightarrow \infty)$. 87,88 P_A and P_B are the populations of A and B states, respectively (P_A + P_B = 1). The lower and upper boundaries for fitting k_{ex} , Φ , and $R_2^{eff}(v_{cpmg} \rightarrow \infty)$ were [1000, 10000], [0, ∞], [0, maximum(R_2^{eff})], respectively. After the fitting, the chemical/conformational exchange contribution to transverse relaxation (R_{ex}) was calculated using (88):

$$R_{ex} \approx \frac{P_A P_B \Delta \omega^2}{k_{ex}} = \frac{\Phi}{k_{ex}}$$
 $(k_{ex} \gg)$

Model 3 refers to the slow exchange ($k_{ex} < d\omega$) between two states, A and B. For model 3, the Carver-Richards equation was used for fitting k_{ex} , P_B , $d\omega$, and $R_2^{eff}(v_{cpmg} \rightarrow \infty)$ (89). The lower and upper boundaries for fitting k_{ex} , P_B , $d\omega$, and $R_2^{eff}(v_{cpmg} \rightarrow \infty)$ were [30, 3000], [0, 0.3], [30, ∞], [0, maximum(R_2^{eff})], respectively. After the fitting, R_{ex} was calculated using:⁸⁸

$$R_{ex} \approx \frac{P_A P_B k_{ex}}{1 + (k_{ex}/\Delta\omega)^2}$$
 $(P_A \gg B)$

Figure Generation

Chemical structures were generated using ChemDraw.⁹⁰ Domain map was generated using IBS.⁹¹ GAP structures were aligned using the "align" command using a sequence-independent algorithm.⁹² Structures were visualized with Pymol (Pymol Molecular Graphics System, Version 2.0 Schrodinger, LLC). PDBsum was used to generate the secondary structure and sequence overlap.⁹³ The APBS plugin was used to visualize electrostatic surfaces (94). Sequence alignments were displayed using PRALINE.⁹⁵

Supplementary Material Description

Supplementary Figure 1: Hydrolysis of GTP is catalyzed through GAP arginine "finger"

Supplementary Figure 2: VopE sequence alignment with other ToxGAPs

Supplementary Table 1: MALS and SAXS scattering values.

Supplementary Figure 3: H¹/N¹⁵ HQSC of VopE.

Supplementary Figure 4: Correlation between calculated and experimental RDC values

Supplementary Figure 5: Sequence and secondary structure alignment

Supplementary Figure 6: Electrostatic Surface Representation of VopE

Supplementary Figure 7: Overlay of VopE fold to that of other ToxGAPs

Supplementary Figure 8: Dispersion curves for the residues with R_{ex} greater than 6 s⁻¹

Supplementary Figure 9: Representative SDS-PAGE and preparative SEC purity for

recombinantly expressed and purified VopE

Author Contributions

K.P.S. initiated and managed the project. K.P.S. expressed and purified proteins. K.P.S. collected, processed, and analyzed SAXS data with assistance from S.C. M.T. collected and processed 3D and relaxation dispersion NMR data. G.C. collected, processed, and analyzed RDC data. W.L. and K.P.S. analyzed NMR data for structure determination and subsequent investigation. Y.L. analyzed all NMR dynamics experiments. S.H.L. and W.L. contributed intellectual input. K.P.S. wrote the manuscript with assistance from W.L. and S.H.L and input from all authors.

<u>Acknowledgements</u>

We thank Cara Gottardi for her support and mentorship. We thank Nick Daffern for advice and suggestions. We thank Ronnie Frederick for relaxation/dispersion sample preparation. We thank Yongbo Zhang, Ishwar Radhakrishnan, and Ryan Marcum for advice on preliminary NMR experiments. We thank Ludmilla Shuvalova and George Minasov for help with preliminary x-ray crystallography data collection. We thank Arabela Grigorescu and Theint Aung for assisting with SEC-MALS data collection. We thank Dileep Varma for use of his laboratory equipment and space. K.P.S. was supported by the Walter S. and Lucienne Driskill Graduate Training Program in Life Sciences at Northwestern University. This study made use of the National Magnetic Resonance Facility at Madison, which is supported by NIH grants P41 GM103399 (NIGMS) and P41 GM66326 (NIGMS). Additional equipment was purchased with funds from the University of Wisconsin, the NIH (RR02181, RR08438), the NSF (DMB-8415048, OIA9977486, BIF-9214394), and the USDA. This study made use of NMRbox: National Center for Biomolecular NMR Data Processing and Analysis, a Biomedical Technology Research Resource (BTRR), which is supported by NIH grant P41GM111135 (NIGMS). This work used resources of the Northwestern University Keck Biophysics Facility, supported by NCI-CCSG-P30-CA060553 awarded to the Robert H. Lurie Comprehensive Cancer Center. Use of the Advanced Photon Source was supported by the US Department of Energy, Office of Science, Office of Basic Energy Sciences, under Contract No. DE-AC02-06CH11357. Use of the BioCAT for SEC-SAXS was supported by APS GUP-49612. Use of the Pilatus 3 1M detector was provided by grant 1S10OD018090-01 from NIGMS. This work has also been supported by the National Science Foundation (DBI-2051595 and DBI-1902076) and the University of Colorado Denver. None of the work included was conducted at Xilio Therapeutics.

Data Deposition

Sequence information is deposited at UniParc under the accession code UPI0004E46228. SAXS data has been submitted to the SASBDB under accession code SASDJV3. NMR data has been deposited to the BMRB under accession code 30756. Structure coordinates have been deposited to the PDB under the accession code 6X6N. All accession codes have been listed in the "Materials and Methods" sections.

References

- 1. CDC. (2021) Cholera Vibrio cholerae infection. General Information.
- 2. Galan JE, Zhou D. Striking a balance: modulation of the actin cytoskeleton by Salmonella. Proc Natl Acad Sci USA. 2000;97:8754-8761.
- 3. Canonne J, Rivas S. Bacterial effectors target the plant cell nucleus to subvert host transcription. Plant Signal Behav. 2012;7:217-221.
- 4. Oswald E, Nougayrede JP, Taieb F, Sugai M. Bacterial toxins that modulate host cell-cycle progression. Curr Opin Microbiol. 2005;8:83-91.
- 5. Finsel I, Ragaz C, Hoffmann C, Harrison CF, Weber S, van Rahden VA, Johannes L, Hilbi H. The Legionella effector RidL inhibits retrograde trafficking to promote intracellular replication. Cell Host Microbe. 2013;14:38-50.
- 6. Jiang JH, Tong J, Gabriel K. Hijacking mitochondria: bacterial toxins that modulate mitochondrial function. IUBMB Life. 2012;64:397-401.
- 7. Stavru F, Palmer AE, Wang C, Youle RJ, Cossart P. Atypical mitochondrial fission upon bacterial infection. Proc Natl Acad Sci USA. 2013;110:16003-16008.
- 8. Stavru F, Cossart P. Listeria infection modulates mitochondrial dynamics. Commun Integr Biol. 2011;4:364-366.
- 9. Escoll P, Song OR, Viana F, Steiner B, Lagache T, Olivo-Marin JC, Impens F, Brodin P, Hilbi H, Buchrieser C. Legionella pneumophila modulates mitochondrial dynamics to trigger metabolic repurposing of infected macrophages. Cell Host Microbe. 2017;22:302-316.
- 10. Rajalingam K, Schreck R, Rapp UR, Albert S. Ras oncogenes and their downstream targets. Biochim Biophys Acta. 2007;1773:1177-1195.
- 11. Kiel C, Filchtinski D, Spoerner M, Schreiber G, Kalbitzer HR, Herrmann C. Improved binding of raf to Ras.GDP is correlated with biological activity. J Biol Chem. 2009;284:31893-31902.
- 12. Block C, Janknecht R, Herrmann C, Nassar N, Wittinghofer A. Quantitative structure-activity analysis correlating Ras/Raf interaction in vitro to Raf activation in vivo. Nat Struct Biol. 1996;3:244-251.
- 13. Tocque B, Delumeau I, Parker F, Maurier F, Multon MC, Schweighoffer F. Ras-GTPase activating protein (GAP): a putative effector for Ras. Cell Signal. 1997;9:153-158.

- 14. Scheffzek K, Ahmadian MR, Kabsch W, Wiesmuller L, Lautwein A, Schmitz F, Wittinghofer A. The Ras-RasGAP complex: structural basis for GTPase activation and its loss in oncogenic Ras mutants. Science. 1997;277:333-338,
- 15. Ahmadian MR, Stege P, Scheffzek K, Wittinghofer A. Confirmation of the arginine-finger hypothesis for the GAP-stimulated GTP-hydrolysis reaction of Ras. Nat Struct Biol. 1997;4:686-689.
- 16. Seewald MJ, Korner C, Wittinghofer A, Vetter IR. RanGAP mediates GTP hydrolysis without an arginine finger. Nature. 2002;415:662-666.
- 17. Pan X, Eathiraj S, Munson M, Lambright DG. TBC-domain GAPs for Rab GTPases accelerate GTP hydrolysis by a dual-finger mechanism. Nature. 2006;442:303-306.
- 18. Amin E, Jaiswal M, Derewenda U, Reis K, Nouri K, Koessmeier KT, Aspenstrom P, Somlyo AV, Dvorsky R, Ahmadian MR. Deciphering the molecular and functional basis of RHOGAP family proteins: A systematic approach toward selective inactivation of RHO family proteins. J Biol Chem. 2016;291:20353-20371.
- 19. Nassar N, Hoffman GR, Manor D, Clardy JC, Cerione RA. Structures of Cdc42 bound to the active and catalytically compromised forms of Cdc42GAP. Nat Struct Biol. 1998;5:1047-1052.
- 20. Hall A. The cellular functions of small GTP-binding proteins. Science. 1990;249:635-640.
- 21. Aktories K, Schmidt G, Just I. Rho GTPases as targets of bacterial protein toxins. Biol Chem. 2000;421-426.
- 22. Popoff MR. Bacterial factors exploit eukaryotic Rho GTPase signaling cascades to promote invasion and proliferation within their host. Small GTPases. 2014;5:e28209.
- 23. Dong N, Zhu Y, Lu Q, Hu L, Zheng Y, Shao F. Structurally distinct bacterial TBC-like GAPs link Arf GTPase to Rab1 inactivation to counteract host defenses. Cell. 2012;150:1029-1041.
- 24. Wurtele M, Wolf E, Pederson KJ, Buchwald G, Ahmadian MR, Barbieri JT, Wittinghofer A. How the Pseudomonas aeruginosa ExoS toxin downregulates Rac. Nat Struct Biol. 2001;8:23-26.
- 25. Yu Q, Hu L, Yao Q, Zhu Y, Dong N, Wang DC, Shao F. Structural analyses of Legionella LepB reveal a new GAP fold that catalytically mimics eukaryotic RasGAP. Cell Res. 2013;23:775-787.

- 26. Evdokimov AG, Tropea JE, Routzahn KM, Waugh DS. Crystal structure of the Yersinia pestis GTPase activator YopE. Protein Sci. 2002;11:401-408.
- 27. Cook WJ, Senkovich O, Chattopadhyay D. Structure of the catalytic domain of Plasmodium falciparum ARF GTPase-activating protein (ARFGAP). Acta Cryst F. 2011;67:1339-1344.
- 28. Alam A, Miller KA, Chaand M, Butler JS, Dziejman M. Identification of Vibrio cholerae type III secretion system effector proteins. Infect Immun. 2011;79:1728-1740.
- 29. Tam VC, Suzuki M, Coughlin M, Saslowsky D, Biswas K, Lencer WI, Faruque SM, Mekalanos JJ. Functional analysis of VopF activity required for colonization in Vibrio cholerae. MBio. 2010;1:e00289-10.
- 30. Shin OS, Tam VC, Suzuki M, Ritchie JM, Bronson RT, Waldor MK, Mekalanos JJ. Type III secretion is essential for the rapidly fatal diarrheal disease caused by non-O1, non-O139 Vibrio cholerae. MBio. 2011;2:e00106-00111.
- 31. Suzuki M, Danilchanka O, Mekalanos JJ. Vibrio cholerae T3SS effector VopE modulates mitochondrial dynamics and innate immune signaling by targeting Miro GTPases. Cell Host Microbe. 2014;16:581-591.
- 32. Tramontano A. Homology modeling with low sequence identity. Methods. 1998;14:293-300.
- 33. Focia PJ, Shepotinovskaya IV, Seidler JA, Freymann DM. Heterodimeric GTPase core of the SRP targeting complex. Science. 2004;303:373-377.
- 34. Chappie JS, Acharya S, Leonard M, Schmid SL, Dyda F. G domain dimerization controls dynamin's assembly-stimulated GTPase activity. Nature. 2010;465:435-440.
- 35. Muratcioglu S, Chavan TS, Freed BC, Jang H, Khavrutskii L, Freed RN, Dyba MA, Stefanisko K, Tarasov SG, Gursoy A, Keskin O, Tarasova NI, Gaponenko V, Nussinov R. GTP-dependent K-Ras dDimerization. Structure. 2015;23:1325-1335.
- 36. Lee W, Stark JL, Markley JL. PONDEROSA-C/S: client-server based software package for automated protein 3D structure determination. J Biomol NMR. 2014;60:73-75.
- 37. Grishaev A, Wu J, Trewhella J, Bax A. Refinement of multidomain protein structures by combination of solution small-angle X-ray scattering and NMR data. J Am Chem Soc. 2005;127:16621-16628.

- 38. Lee W, Cornilescu G, Dashti H, Eghbalnia HR, Tonelli M, Westler WM, Butcher SE, Henzler-Wildman KA, Markley JL. Integrative NMR for biomolecular research. J Biomol NMR. 2016;64:307-332,
- 39. Ulrich EL, Akutsu H, Doreleijers JF, Harano Y, Ioannidis YE, Lin J, Livny M, Mading S, Maziuk D, Miller Z, Nakatani E, Schulte CF, Tolmie DE, Kent Wenger R, Yao H, Markley JL. BioMagResBank. Nucleic Acids Res. 2008;36:D402-408,
- 40. Berman HM, Westbrook J, Feng Z, Gilliland G, Bhat TN, Weissig H, Shindyalov IN, Bourne PE. The Protein Data Bank. Nucleic Acids Res. 2000;28:235-242.
- 41. Wurtele M, Renault L, Barbieri JT, Wittinghofer A, Wolf E. Structure of the ExoS GTPase activating domain. FEBS Lett. 2001;491:26-29.
- 42. Stebbins CE, Galan JE. Modulation of host signaling by a bacterial mimic: structure of the Salmonella effector SptP bound to Rac1. Mol Cell. 2000;6:1449-1460.
- 43. Loria JP, Rance R, Palmer AG. A relaxation-compensated Carr– Purcell– Meiboom– Gill sequence for characterizing chemical exchange by NMR spectroscopy. J Am Chem Soc. 1999;121:2331-2332.
- 44. Eathiraj S, Pan X, Ritacco C, Lambright DG. Structural basis of family-wide Rab GTPase recognition by rabenosyn-5. Nature. 2005;436:415-419.
- 45. Tang BL. MIRO GTPases in mitochondrial transport, homeostasis and pathology. Cells. 2015;5:1.
- 46. Marks B, Stowell MH, Vallis Y, Mills IG, Gibson A, Hopkins CR, McMahon HT. GTPase activity of dynamin and resulting conformation change are essential for endocytosis. Nature. 2001;410:231-235.
- 47. Fransson S, Ruusala A, Aspenstrom P. The atypical Rho GTPases Miro-1 and Miro-2 have essential roles in mitochondrial trafficking. Biochem Biophys Res Commun. 2006;344:500-510.
- 48. Seitz S, Kwon Y, Hartleben G, Julg J, Sekar R, Krahmer N, Najafi B, Loft A, Gancheva S, Stemmer K, Feuchtinger A, Hrabe de Angelis M, Muller TD, Mann M, Bluher M, Roden M, Berriel Diaz M, Behrends C, Gilleron J, Herzig S, Zeigerer A. Hepatic Rab24 controls blood glucose homeostasis via improving mitochondrial plasticity. Nat Metab. 2019;1:1009-1026.
- 49. Bui M, Gilady SY, Fitzsimmons RE, Benson MD, Lynes EM, Gesson K, Alto NM, Strack S, Scott JD, Simmen T. Rab32 modulates apoptosis onset and mitochondria-associated membrane (MAM) properties. J Biol Chem. 2010;285:31590-31602.

- 50. Shlevkov E, Kramer T, Schapansky J, LaVoie MJ, Schwarz TL. Miro phosphorylation sites regulate Parkin recruitment and mitochondrial motility. Proc Natl Acad Sci USA. 2016;113:E6097-E6106.
- 51. Klosowiak JL, Park S, Smith KP, French ME, Focia PJ, Freymann DM, Rice SE. Structural insights into Parkin substrate lysine targeting from minimal Miro substrates. Sci Rep. 2016;6:33019.
- 52. Agarwal S, Smith KP, Zhou Y, Suzuki A, McKenney RJ, Varma D. Cdt1 stabilizes kinetochore-microtubule attachments via an Aurora B kinase-dependent mechanism. J Cell Biol. 2018;217:3446-3463.
- Peng Z, Kurgan L. On the complementarity of the consensus-based disorder prediction. Pac Symp Biocomput. 2012;176-187.
- 54. Fan X, Kurgan L. Accurate prediction of disorder in protein chains with a comprehensive and empirically designed consensus. J Biomol Struct Dyn. 2014;32:448-464.
- 55. McGuffin LJ, Bryson K, Jones DT. The PSIPRED protein structure prediction server. Bioinformatics. 2000;16:404-405.
- 56. Dosztanyi Z, Csizmok V, Tompa P, Simon I. IUPred: web server for the prediction of intrinsically unstructured regions of proteins based on estimated energy content. Bioinformatics. 2005;21:3433-3434.
- 57. Obradovic Z, Peng K, Vucetic S, Radivojac P, Brown CJ, Dunker AK. Predicting intrinsic disorder from amino acid sequence. Proteins. 2003;53:566-572.
- 58. Linding R, Jensen LJ, Diella F, Bork P, Gibson TJ, Russell RB. Protein disorder prediction: implications for structural proteomics. Structure. 2003;11:1453-1459.
- 59. Sormanni P, Camilloni C, Fariselli P, Vendruscolo M. The s2D method: simultaneous sequence-based prediction of the statistical populations of ordered and disordered regions in proteins. J Mol Biol. 2015;427:982-996.
- 60. Walsh I, Martin AJ, Di Domenico T, Tosatto SC. ESpritz: accurate and fast prediction of protein disorder. Bioinformatics. 2012;28:503-509.
- 61. Rost B, Sander C. Combining evolutionary information and neural networks to predict protein secondary structure. Proteins. 1994;19:55-72.
- 62. Lin K, Simossis VA, Taylor WR, Heringa J. A simple and fast secondary structure prediction method using hidden neural networks. Bioinformatics. 2005;21:152-159.

- 63. UniProt C. Activities at the Universal Protein Resource (UniProt). Nucleic Acids Res. 2014;42:D191-198.
- 64. Altschul SF, Gish W, Miller W, Myers EW, Lipman DJ. Basic local alignment search tool. J Mol Biol. 1990;215:403-410.
- 65. Gasteiger E., H. C., Gattiker A., Duvaud S., Wilkins M.R., Appel R.D., Bairoch A. (2005) Protein Identification and Analysis Tools on the ExPASy Server, Humana Press, Totowa, NJ.
- 66. Mathew E, Mirza A, Menhart N. Liquid-chromatography-coupled SAXS for accurate sizing of aggregating proteins. J Synchrotron Radiat. 2004;11:314-318.
- 67. Valentini E, Kikhney AG, Previtali G, Jeffries CM, Svergun DI. SASBDB, a repository for biological small-angle scattering data. Nucleic Acids Res. 2015;43:D357-363.
- 68. Fazio VJ, Peat TS, Newman J. A drunken search in crystallization space. Acta Cryst F. 2014;70:1303-1311.
- 69. Delaglio F, Grzesiek S, Vuister GW, Zhu G, Pfeifer J, Bax A. NMRPipe: a multidimensional spectral processing system based on UNIX pipes. J Biomol NMR. 1995;6:277-293.
- 70. Hyberts SG, Takeuchi K, Wagner G. Poisson-gap sampling and forward maximum entropy reconstruction for enhancing the resolution and sensitivity of protein NMR data. J Am Chem Soc. 2010;132:2145-2147.
- 71. Ying J, Delaglio F, Torchia DA, Bax A. Sparse multidimensional iterative lineshape-enhanced (SMILE) reconstruction of both non-uniformly sampled and conventional NMR data. J Biomol NMR. 2017;68:101-118.
- 72. Fitzkee NC, Bax A. Facile measurement of (1)H-(1)5N residual dipolar couplings in larger perdeuterated proteins. J Biomol NMR. 2010;48:65-70.
- 73. Maciejewski MW, Schuyler AD, Gryk MR, Moraru II, Romero PR, Ulrich EL, Eghbalnia HR, Livny M, Delaglio F, Hoch JC. NMRbox: A resource for biomolecular NMR computation. Biophys J. 2017;112:1529-1534.
- 74. Lee W, Tonelli M, Markley JL. NMRFAM-SPARKY: enhanced software for biomolecular NMR spectroscopy. Bioinformatics. 2015;31:1325-1327.
- 75. Shin J, Lee W, Lee W. Structural proteomics by NMR spectroscopy. Expert Rev Proteomics. 2008;5:589-601.

- 76. Lee W, Bahrami A, Dashti HT, Eghbalnia HR, Tonelli M, Westler WM, Markley JL. I-PINE web server: an integrative probabilistic NMR assignment system for proteins. J Biomol NMR. 2019;73:213-222.
- 77. Lee W, Markley JL. PINE-SPARKY.2 for automated NMR-based protein structure research. Bioinformatics. 2018;34:1586-1588.
- 78. Eghbalnia HR, Wang L, Bahrami A, Assadi A, Markley JL. Protein energetic conformational analysis from NMR chemical shifts (PECAN) and its use in determining secondary structural elements. J Biomol NMR. 2005;32:71-81.
- 79. Lee W, Yu W, Kim S, Chang I, Lee W, Markley JL. PACSY, a relational database management system for protein structure and chemical shift analysis. J Biomol NMR. 2012;54:169-179.
- 80. Schwieters CD, Kuszewski JJ, Tjandra N, Clore GM. The Xplor-NIH NMR molecular structure determination package. J Magn Reson. 2003;160:65-73.
- 81. Lee W, Petit CM, Cornilescu G, Stark JL, Markley JL. The AUDANA algorithm for automated protein 3D structure determination from NMR NOE data. J Biomol NMR. 2016;65:51-57.
- 82. Lee W, Kim JH, Westler WM, Markley JL. PONDEROSA, an automated 3D-NOESY peak picking program, enables automated protein structure determination. Bioinformatics. 2011;27:1727-1728.
- 83. Guntert P. Automated NMR structure calculation with CYANA. Methods Mol Biol. 2004;278:353-378.
- 84. Mattinen ML, Paakkonen K, Ikonen T, Craven J, Drakenberg T, Serimaa R, Waltho J, Annila A. Quaternary structure built from subunits combining NMR and small-angle x-ray scattering data. Biophys J. 2002;83:1177-1183.
- 85. Sunnerhagen M, Olah GA, Stenflo J, Forsen S, Drakenberg T, Trewhella J. The relative orientation of Gla and EGF domains in coagulation factor X is altered by Ca2+ binding to the first EGF domain. A combined NMR small angle X-ray scattering study. Biochemistry. 1996;35:11547-11559.
- 86. Bhattacharya A, Tejero R, Montelione GT. Evaluating protein structures determined by structural genomics consortia. Proteins. 2007;66:778-795.
- 87. Luz Z, Meiboom S. Nuclear magnetic resonance study of the protolysis of trimethylammonium ion in aqueous solution—order of the reaction with respect to solvent. J Chem Phys. 1963;39:366.

- 88. Millet O, Loria JP, Kroenke CD, Pons M, Palmer AG. The static magnetic field dependence of chemical exchange linebroadening defines the NMR chemical shift time scale. J Am Chem Soc. 2000;122:2867-2877.
- 89. Carver JP, Richards RE. A general two-site solution for the chemical exchange produced dependence of T2 upon the carr-Purcell pulse separation. J Magn Reson. 1972;6:89-105.
- 90. Cousins KR. Computer review of ChemDraw Ultra 12.0. J Am Chem Soc. 2011;133:8388.
- 91. Liu W, Xie Y, Ma J, Luo X, Nie P, Zuo Z, Lahrmann U, Zhao Q, Zheng Y, Zhao Y, Xue Y, Ren J. IBS: an illustrator for the presentation and visualization of biological sequences. Bioinformatics. 2015;31:3359-3361.
- 92. Holm L, Sander C. Protein structure comparison by alignment of distance matrices. J Mol Biol. 1993;233:123-138.
- 93. Laskowski RA, Jablonska J, Pravda L, Varekova RS, Thornton JM. PDBsum: Structural summaries of PDB entries. Protein Sci. 2018;27:129-134.
- 94. Baker NA, Sept D, Joseph S, Holst MJ, McCammon JA. Electrostatics of nanosystems: application to microtubules and the ribosome. Proc Natl Acad Sci USA. 2001;98:10037-10041.
- 95. Simossis VA, Heringa J. PRALINE: a multiple sequence alignment toolbox that integrates homology-extended and secondary structure information. Nucleic Acids Res. 2005;33:W289-294.

Figure Legends

<u>Figure 1</u>: VopE domain organization. Amino acid number is labeled below. In green, the mitochondrial targeting sequence (MTS), in light blue, the unknown domain, and in blue, the putative GTPase Activating Protein (GAP) domain. Putative catalytic residue Arg125 and putative guanosine interacting residue Thr164 are labeled.

<u>Figure 2</u>: VopE SEC-MALS and SEC-SAXS characterization. A) SEC-MALS chromatogram of VopE and standards. On the x-axis is elution volume and on the y-axis are normalized differential refractive index and molecular weight. VopE is shown in blue and BSA/carbonic anhydrase are shown in red, with molecular weight shown in black. The theoretical molecular weights of BSA (66.5 kDa), carbonic anhydrase (30.0 kDa), and VopE (14.9 kDa) agree well to the calculated molecular weights. B) Raw scattering. I(q) is plotted as a function of q. C) Guinier plot. Ln(I(q)) is plotted as function of q^2 . D) Particle distribution function. P(r) is plotted as a function of r. E) Kratky plot. $I(q)^*q$ squared is plotted as a function of q.

<u>Figure 3</u>: NMR Structure of VopE GAP domain. A) Lowest 20 energy calculated structures. Three different angles are shown, each rotated by 90 degrees as indicated by arrows. B) SAXS electron density overlapping with lowest energy structure. The SAXS *ab initio* space-filling model is shown in grey translucent spheres while VopE is shown in blue cartoon representation.

<u>Figure 4</u>: VopE GAP domain elements. A) VopE in cylinder representation. N- and C-terminus labeled and on the bottom of the molecule as "N" and "C". Alpha helices are labeled $\alpha 1$ -7, and Bulge1 and Bulge 2 are indicated with lines. Note the protein secondary structure is primarily alpha helical, with long "linker' regions between helices. Putative catalytic arginine and ribose-binding threonine are shown in sticks. B) VopE backbone shown in blue wire. Putative GTP-binding Arg125 and Thr164 shown in sticks and colored according to element. C) VopE is shown in blue. YopE is shown in light green. Proteins shown in cylinder representation and rotated 90°. RMSD = 4.831Å. D) Overlay of VopE NMR ensemble, shown in blue, and YopE crystal structure, shown in green. Note the displacement of the helices and difference in secondary structure.

<u>Figure 5</u>: VopE conformational dynamics from NMR relaxation dispersion data. A) plot of Rex as a function of residue number. Residues with Re greater than 6 s⁻¹ are labeled. R_{ex} values of each amide proton were acquired by analyzing CPMG relaxation dispersion data. B) Overlay of VopE NMR structure, shown in blue, and YopE crystal structure, shown in green. Residues of VopE-GAP with R_{ex} greater than 6 s⁻¹ are shown as red spheres. C) ExoS/Rac1 co-crystal structure (PDB ID: 1HE1) overlaid with VopE. VopE shown in blue, ExoS shown in light blue, and Rac shown in dark grey. GTP, AlF3, and residues involved in GTP catalysis or coordination are shown as sticks. Magnesium ion shown as a sphere. GTP and AlF3 are colored by element, ExoS residues are shown in red, and corresponding VopE residues are shown in orange.

Protein Science Page 38 of 53

<u>Table 1</u>: NMR and refinement statistics for VopE

^aStructure statistics were calculated using the 20 lowest pseudo-potential energy conformers out of the 100 total calculated conformers. The average pairwise RMSD was calculated against the lowest-energy conformer.

^bRMSD and Ramachandran statistics were obtained using ordered VopE residues 88-204 as defined by Xplor.

NMR constraints and structure statistics (VopE 88-	<u>Value</u>
204)	
<u>Distance constraints</u>	
Total NOE	2492
Short-range ($ i-j \le 1$)	1482
Medium-range (1 < i − j ≤ 5)	617
Long-range (i – j > 5)	266
Hydrogen bonds	127
<u>Dihedral angle restraints</u>	
Total	200
ф	101
ψ	99
Structure statistics ^a	
<u>Violations</u>	
Distance constraints (>0.5 Å)	0
Dihedral angle constraints (>5°)	0
Van der Waals (>0.2 Å)	0
Average pairwise RMSDb (Å)	
Heavy	0.85 ± 0.27
Backbone	0.58 ± 0.24
Xplor-NIH pseudopotential energy (kJ mol ⁻¹)	12194
MOLPROBITY mean score/clash score	1.36/16.79
MOLPROBITY Ramachandran plot summary ^b (%)	
Favored regions	96.2
Allowed regions	3.1
Disallowed regions	0.7

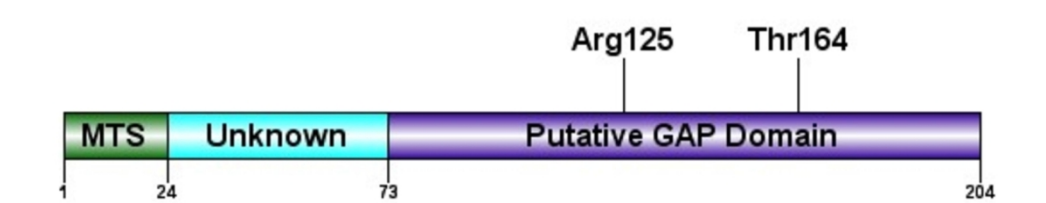


Figure 1: VopE domain organization. Amino acid number is labeled below. In green, the mitochondrial targeting sequence (MTS), in light blue, the unknown domain, and in blue, the putative GTPase Activating Protein (GAP) domain. Putative catalytic residue Arg125 and putative guanosine interacting residue Thr164 are labeled.

144x38mm (300 x 300 DPI)

Protein Science Page 40 of 53

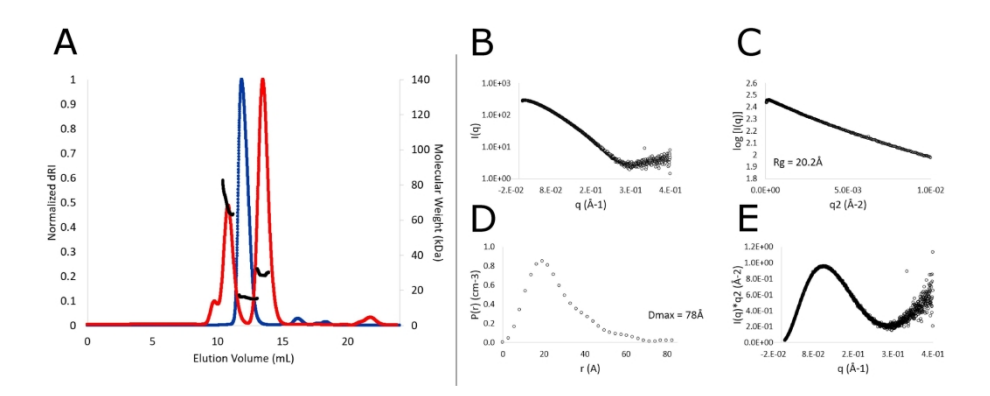


Figure 2: VopE SEC-MALS and SEC-SAXS characterization. A) SEC-MALS chromatogram of VopE and standards. On the x-axis is elution volume and on the y-axis are normalized differential refractive index and molecular weight. VopE is shown in blue and BSA/carbonic anhydrase are shown in red, with molecular weight shown in black. The theoretical molecular weights of BSA (66.5 kDa), carbonic anhydrase (30.0 kDa), and VopE (14.9 kDa) agree well to the calculated molecular weights. B) Raw scattering. I(q) is plotted as a function of q. C) Guinier plot. Ln(I(q)) is plotted as function of q2. D) Particle distribution function. P(r) is plotted as a function of r. E) Kratky plot. I(q)*q squared is plotted as a function of q.

210x75mm (300 x 300 DPI)

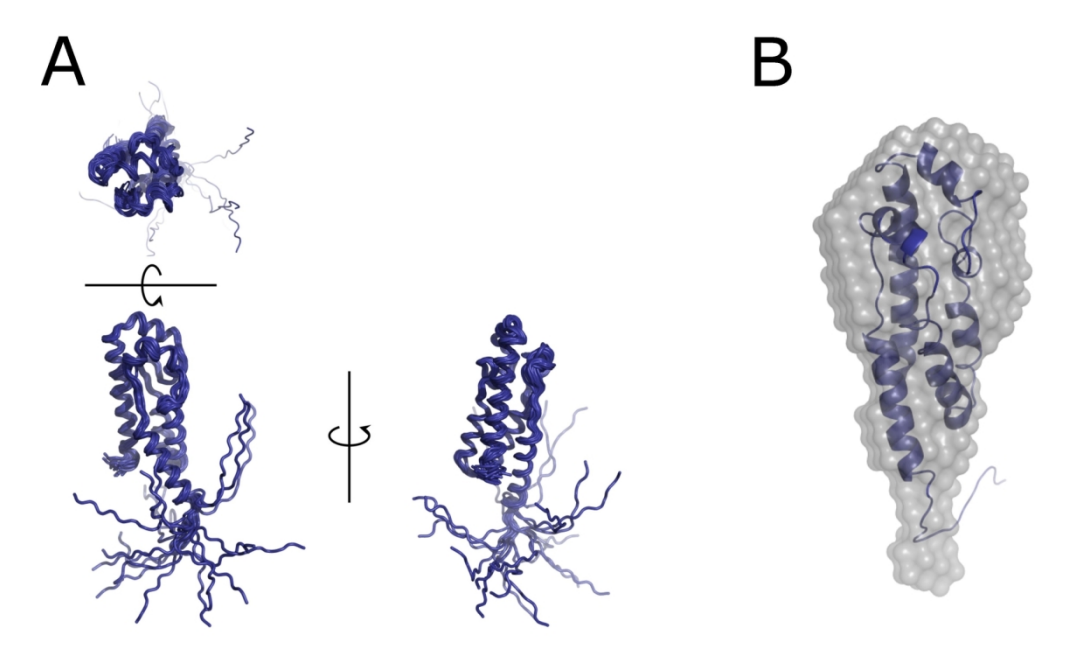


Figure 3: NMR Structure of VopE GAP domain. A) Lowest 20 energy calculated structures. Three different angles are shown, each rotated by 90 degrees as indicated by arrows. B) SAXS electron density overlapping with lowest energy structure. The SAXS ab initio space-filling model is shown in grey translucent spheres while VopE is shown in blue cartoon representation.

157x95mm (300 x 300 DPI)

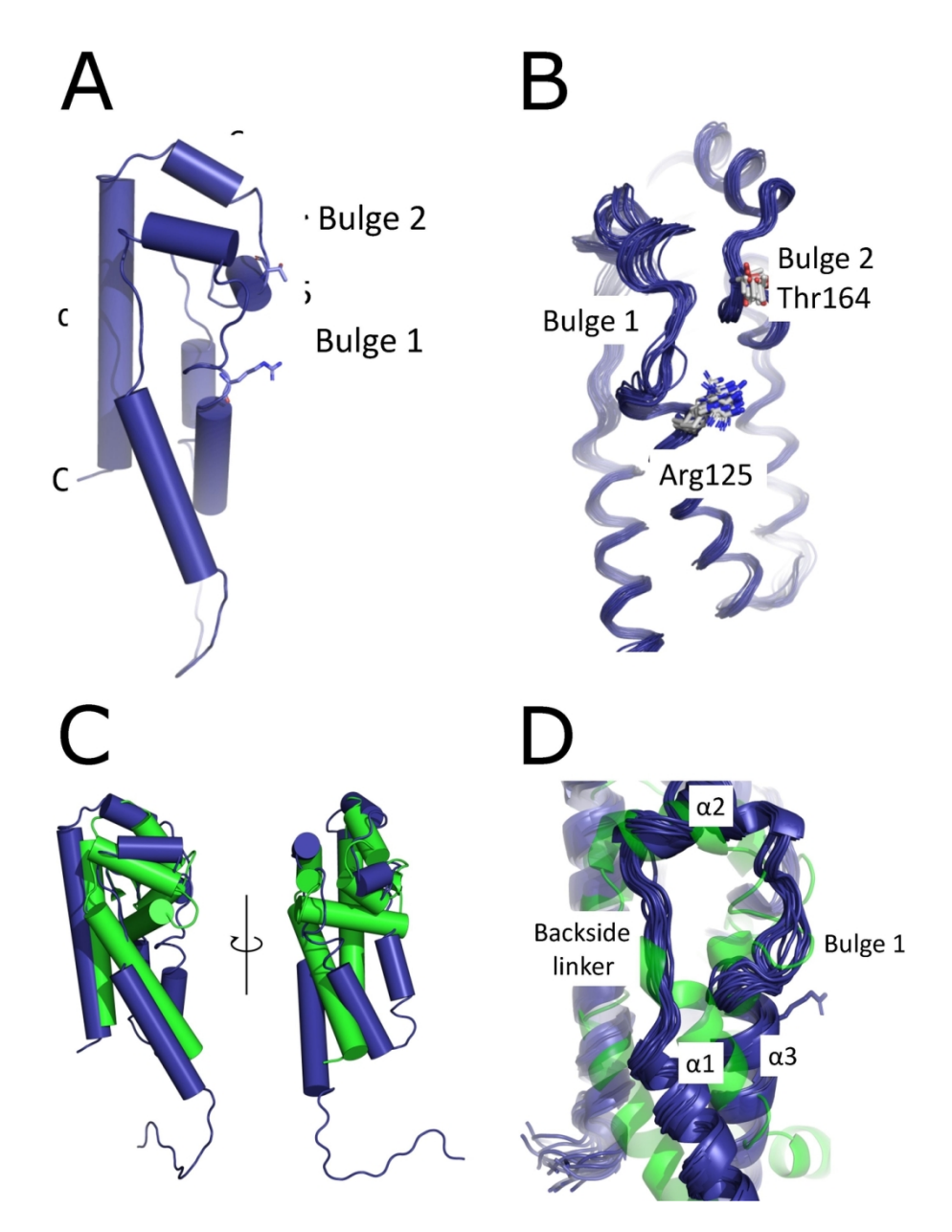


Figure 4: VopE GAP domain elements. A) VopE in cylinder representation. N- and C-terminus labeled and on the bottom of the molecule as "N" and "C". Alpha helices are labeled a1-7, and Bulge1 and Bulge 2 are indicated with lines. Note the protein secondary structure is primarily alpha helical, with long "linker' regions between helices. Putative catalytic arginine and ribose-binding threonine are shown in sticks. B) VopE backbone shown in blue wire. Putative GTP-binding Arg125 and Thr164 shown in sticks and colored according to element. C) VopE is shown in blue. YopE is shown in light green. Proteins shown in cylinder representation and rotated 90°. RMSD = 4.831Å. D) Overlay of VopE NMR ensemble, shown in blue, and YopE crystal structure, shown in green. Note the displacement of the helices and difference in secondary structure.

117x153mm (300 x 300 DPI)

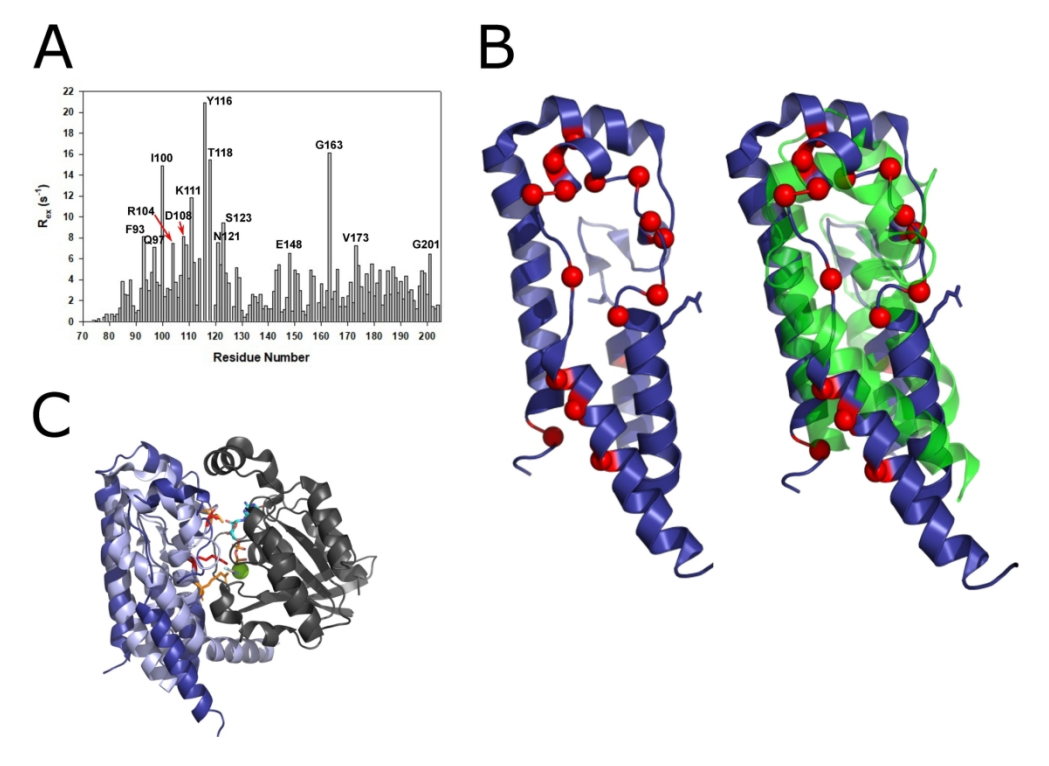


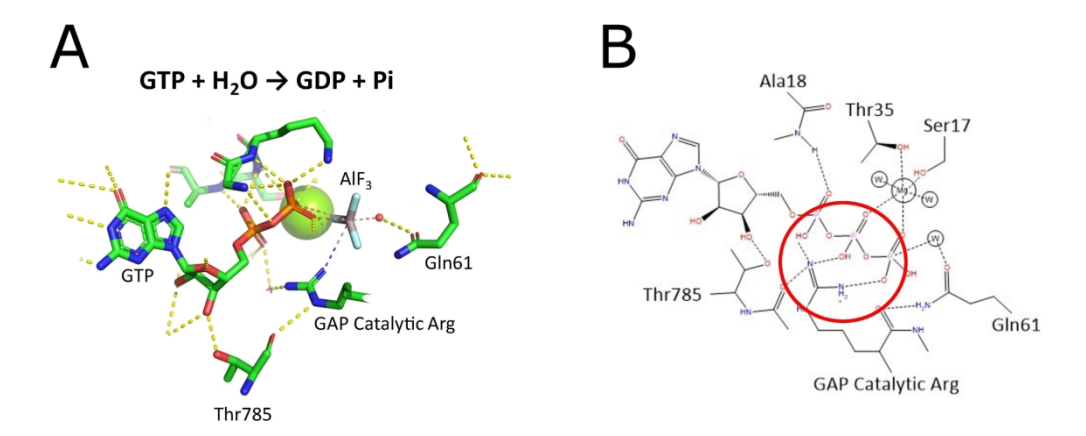
Figure 5: VopE conformational dynamics from NMR relaxation dispersion data. A) plot of Rex as a function of residue number. Residues with Re greater than 6 s-1 are labeled. Rex values of each amide proton were acquired by analyzing CPMG relaxation dispersion data. B) Overlay of VopE NMR structure, shown in blue, and YopE crystal structure, shown in green. Residues of VopE-GAP with Rex greater than 6 s-1 are shown as red spheres. C) ExoS/Rac1 co-crystal structure (PDB ID: 1HE1) overlaid with VopE. VopE shown in blue, ExoS shown in light blue, and Rac shown in dark grey. GTP, AIF3, and residues involved in GTP catalysis or coordination are shown as sticks. Magnesium ion shown as a sphere. GTP and AIF3 are colored by element, ExoS residues are shown in red, and corresponding VopE residues are shown in orange.

176x125mm (300 x 300 DPI)

<u>Supplementary Table 1</u>: MALS and SAXS scattering values.

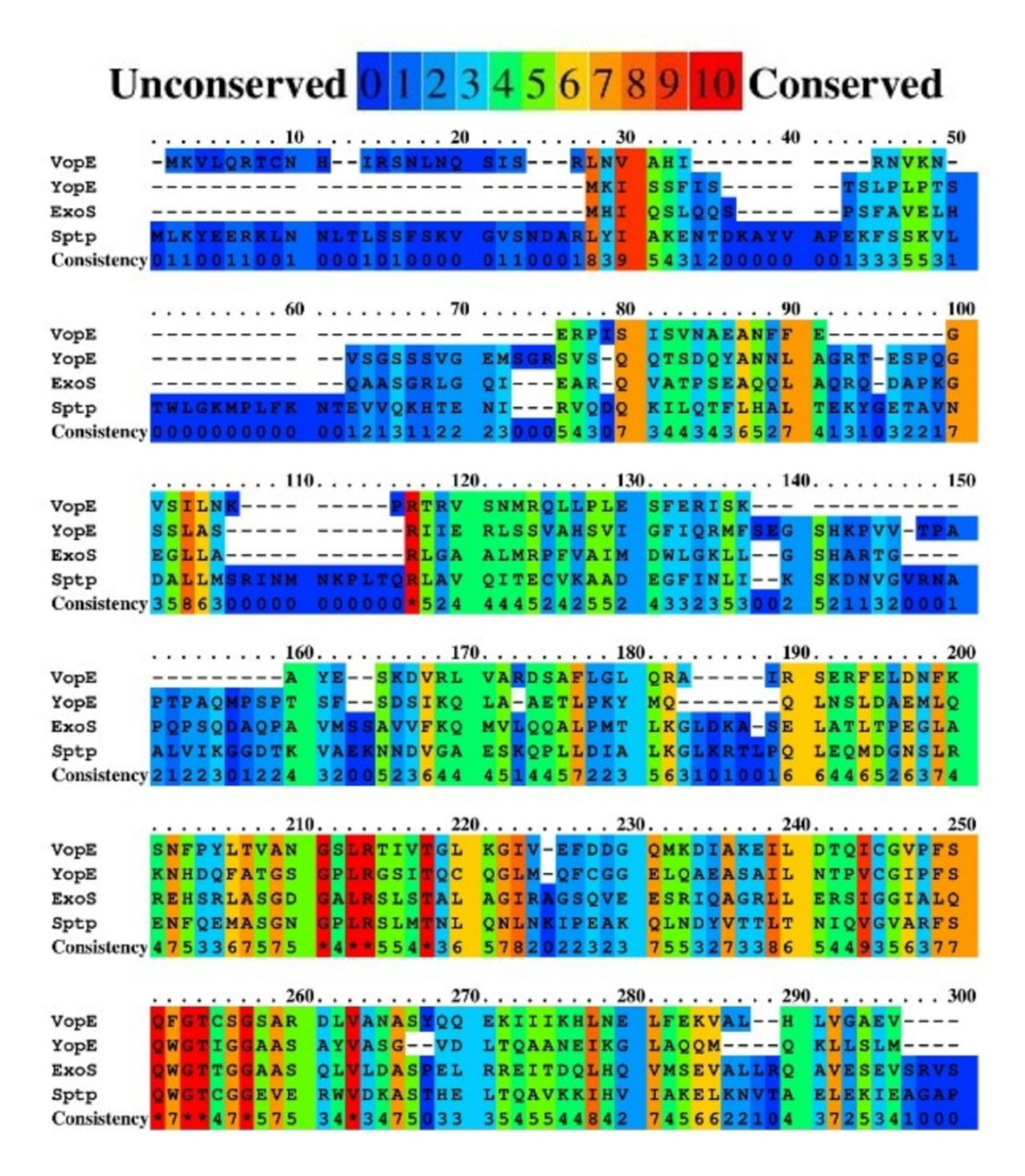
Parameter	Value
QELS R(h) (Å)	20.1 <u>+</u> 0.6
X-ray Wavelength (Å)	1.033
Rg (Å)	20.2 <u>+</u> 0.1
R(h)/Rg (QELS and SAXS)	1
Dmax (Å)	78
Porod Volume (Ų)	23,602
Total Estimate from GNOM	0.731
Number of DAMMIF	10
Reconstructions	
NSD of DAMMIF Reconstructions	0.563
CRYSOL x ²	1.47
Theoretical MW (kDa)	14.9
Calculated MW MALS (kDa)	15.8
Calculated MW SAXS (kDa)	14.8

Page 45 of 53 Protein Science



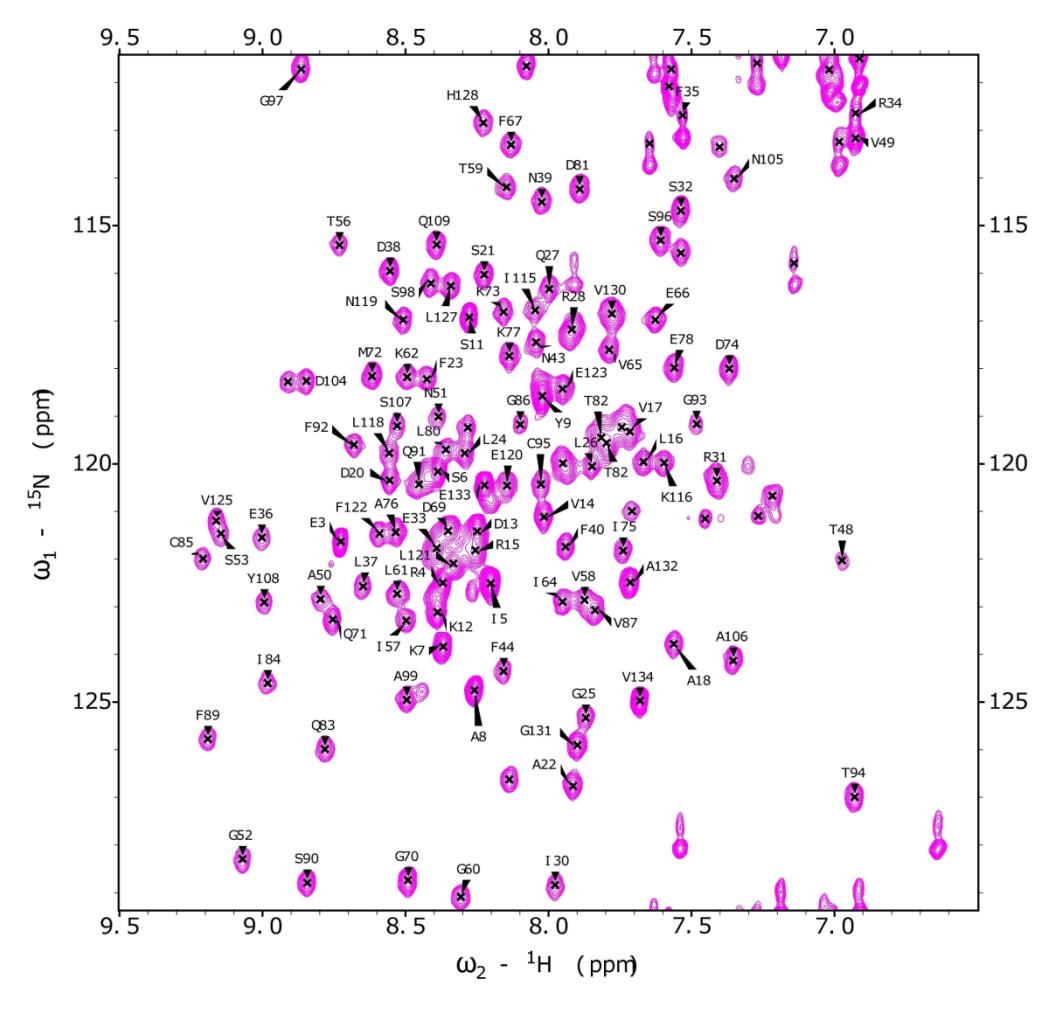
Supplementary Figure 1: Hydrolysis of GTP is catalyzed through GAP arginine "finger". A) Ras/RasGAP active site (PDB ID: 1WQ1). Side chains, GTP, and AIF3 are shown as sticks. Magnesium ion shown as large sphere. Catalytic water shown as small sphere. Hydrogen bonds are shown in yellow, dashed lines.B) 2D representation of active site. Carbons, magnesium ions, and waters are shown in black. Nitrogens are shown in blue. Oxygens are shown in red. Phosphates are shown in pink. Numbering is according to Ras/RasGAP residues. Only residues involved in magnesium coordination or GTP catalysis are shown.

178x70mm (300 x 300 DPI)



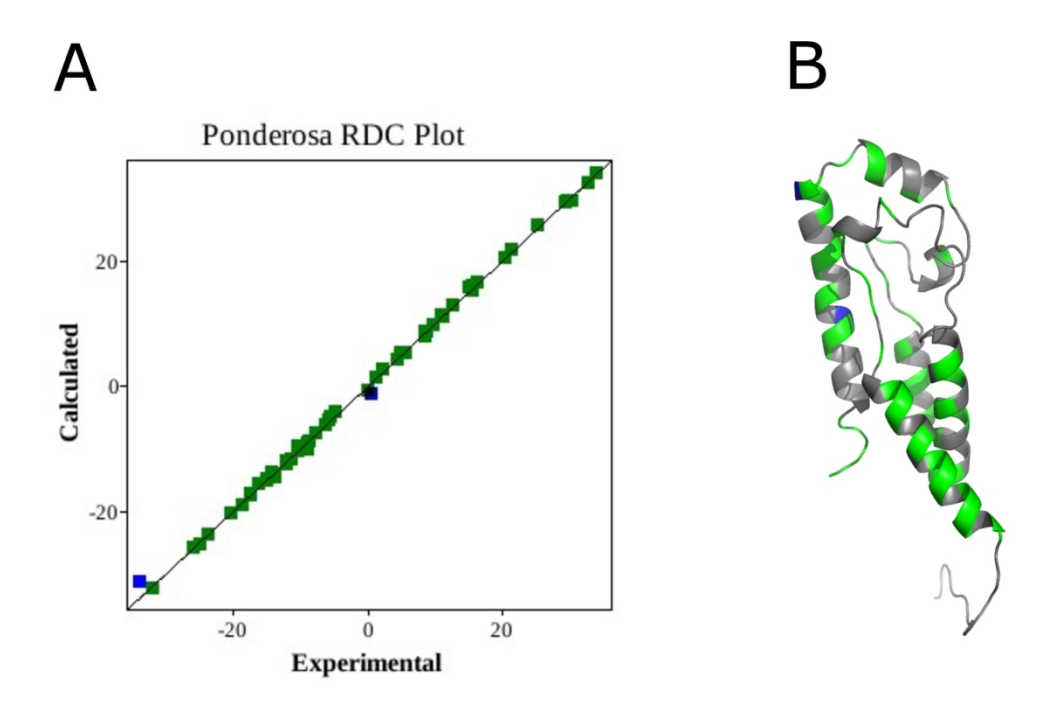
Supplementary Figure 2: VopE sequence alignment with other ToxGAPs. B) Alignment of VopE with other known ToxGAPs. The boxed arginine residue is putative catalytic "arginine finger" and boxed threonine residue is predicted to be GTP-binding. Residue numbers are from the consensus alignment. YopE is 34% identical, ExoS is 29% identical, and Sptp is 27% identical to VopE.

183x215mm (300 x 300 DPI)



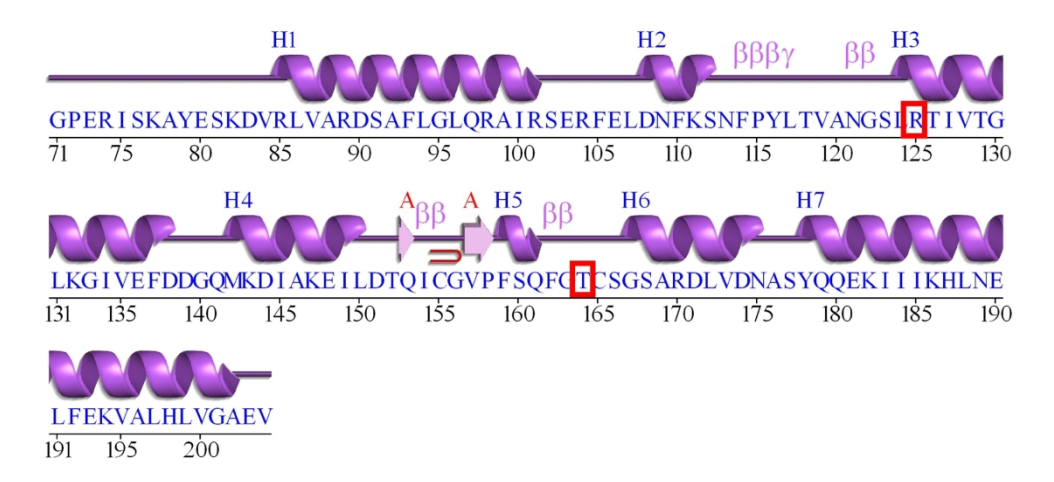
Supplementary Figure 3: H1/N15 HQSC of VopE. 192x183mm~(300~x~300~DPI)

Protein Science Page 48 of 53



Supplementary Figure 4: Correlation between calculated and experimental RDC values. Correlation between calculated and experimental RDC values. A) Experimental RDC values plotted against calculated RDC values. Green corresponds to good agreement, blue corresponds to acceptable agreement, and red corresponds to disagreement. B) RDC correlations plotted onto lowest energy VopE structure, with same coloring scheme as in A.

161x104mm (300 x 300 DPI)

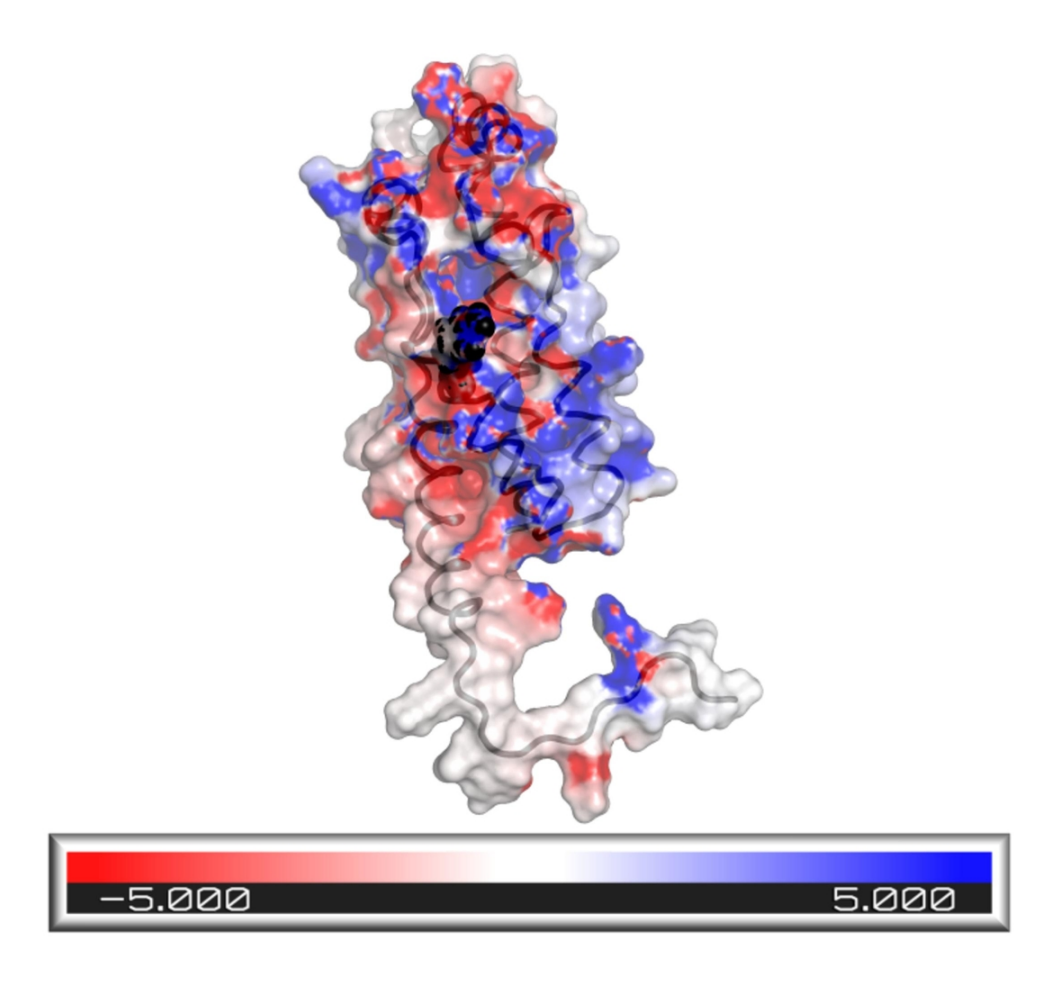


Supplementary Figure 5: Sequence and secondary structure alignment. Residue number is aligned with secondary structural element from lowest energy NMR structure. Alpha helices 1-7 are labeled H1-7.

Conserved threonine and arginine residues highlighted in red boxes.

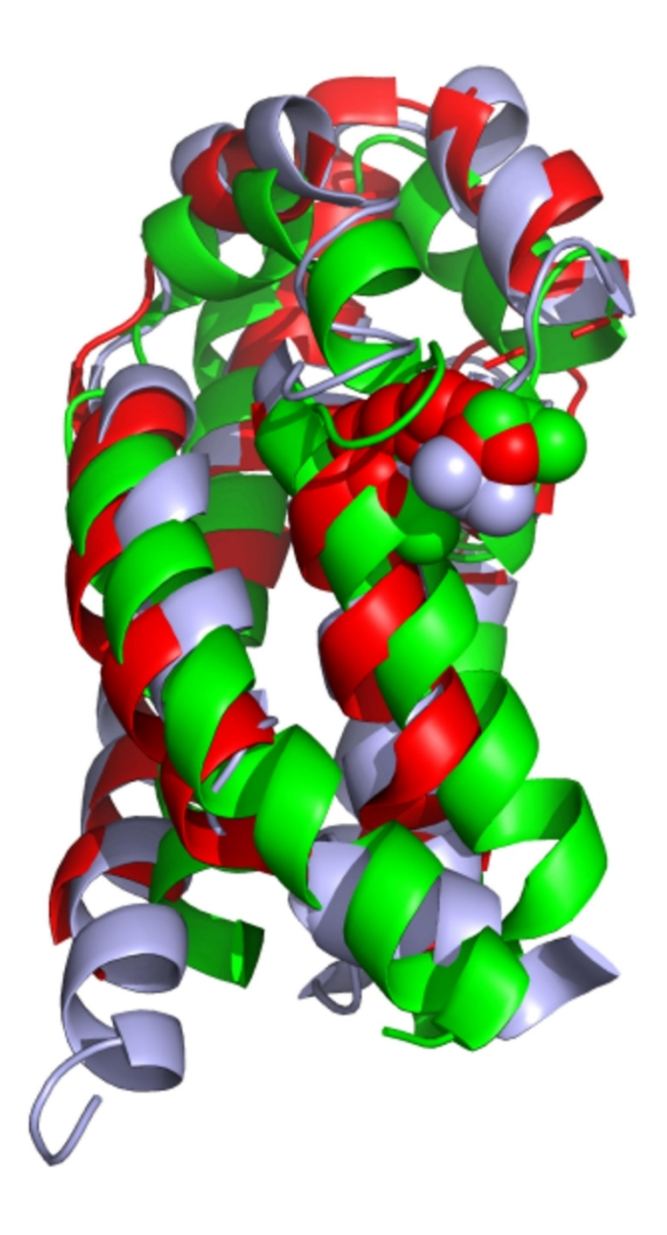
182x81mm (300 x 300 DPI)

Protein Science Page 50 of 53



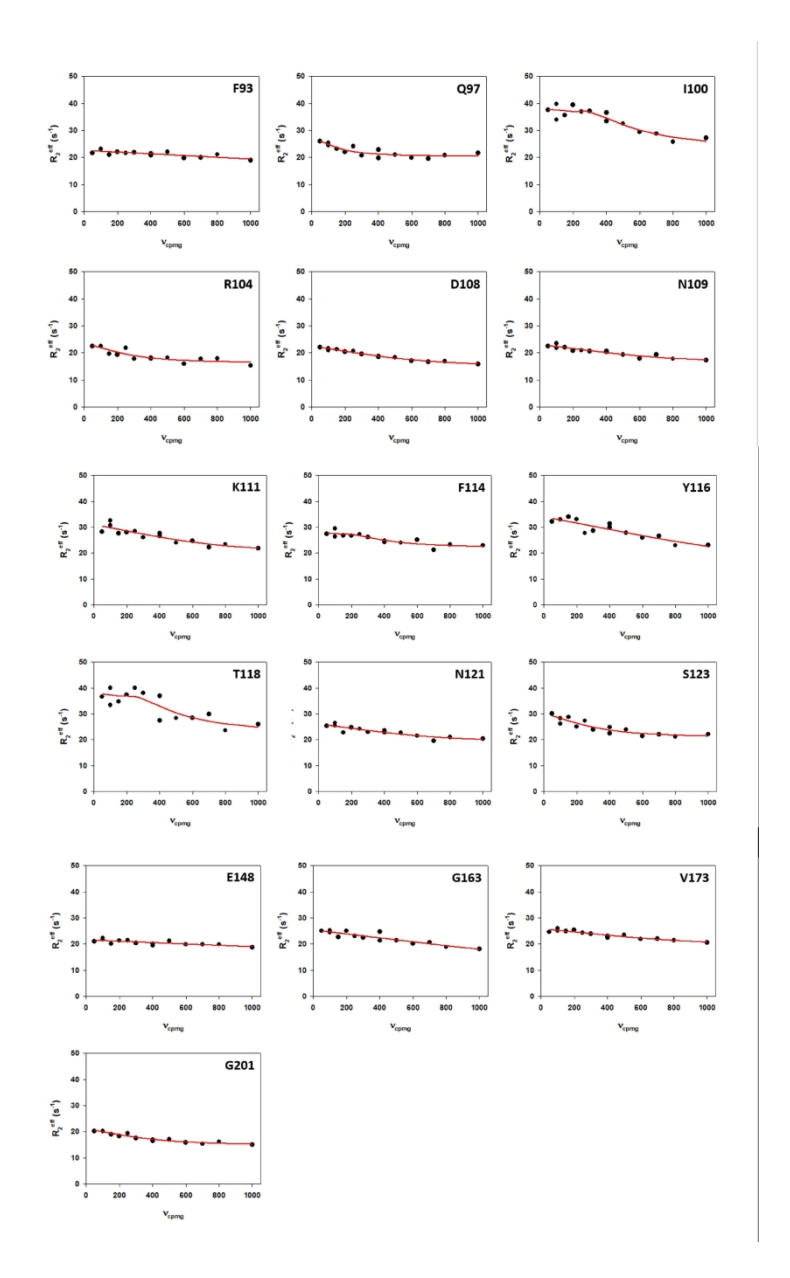
Supplementary Figure 6: Electrostatic Surface Representation of VopE. VopE is shown in ribbon and surface representations. Putative catalytic Arg125 shown in spheres and circled. Backbone and Arg125 shown in black and surface colored according to APBS scheme where red is acidic and blue is basic.

94x86mm (300 x 300 DPI)



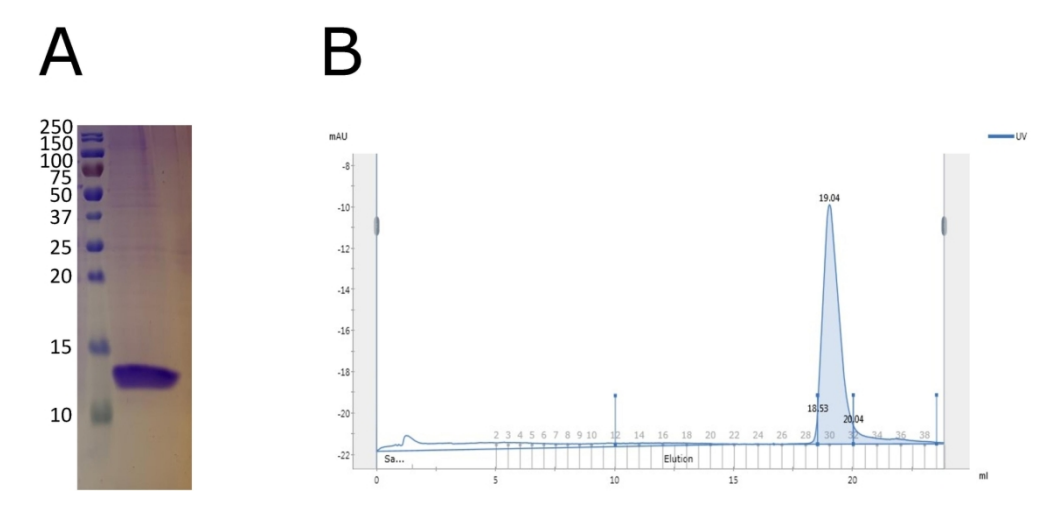
Supplementary Figure 7: Overlay of VopE fold to that of other ToxGAPs. YopE crystal structure (PDB ID: 1HY5) is shown in light green. ExoS lowest energy NMR structure (PDB ID:1HE9) is shown in light blue. Sptp crystal structure (PDB ID:1G4W) is shown in red. The protein backbones are shown in cartoon representation, while the catalytic arginine residues are shown in spheres.

69x120mm (300 x 300 DPI)



Supplementary Figure 8: Dispersion curves for the residues with Rex greater than 6 s-1. R2 eff (s-1) are shown as a function of vcpmg.

165x267mm (300 x 300 DPI)



Supplementary Figure 9: Representative SDS-PAGE and preparative SEC purity for recombinantly expressed and purified VopE. A) SDS-PAGE of purified VopE. The theoretical weight of the construct in 14.9 kDa. B) Preparative FPLC-SEC chromatogram. Abs280 is plotted as a function of elution volume. Highlighted fractions 29-32 were pooled for final protein.

160x74mm (300 x 300 DPI)